

Review

Drag Losses of Wet Brakes and Clutches—A Scoping Review

Lukas Pointner-Gabriel *, Katharina Voelkel and Karsten Stahl 

Gear Research Center (FZG), Department of Mechanical Engineering, School of Engineering & Design, Technical University of Munich, 85748 Garching near Munich, Germany

* Correspondence: lukas.pointner-gabriel@tum.de

Abstract: Wet brakes and clutches are crucial drivetrain components widely used in many sectors. However, their drag losses can account for a considerable share of the overall drivetrain losses. Therefore, investigation of the drag loss behavior of wet brakes and clutches has been the subject of research since the 1970s. This paper aims to provide a comprehensive overview of existing knowledge of drag loss behavior and identify future research directions. To this end, a scoping review was conducted according to the PRISMA guideline. It was found that research mainly, but not only, focused on gaining a fundamental understanding of the drag loss generation process, investigating the integral drag loss behavior, analyzing the flow in the sub-millimeter gaps, and modeling and calculating the drag losses. The review summarizes the state of the art and may support researchers and engineers in developing low-loss wet brake and clutch systems. Several research gaps were identified and are provided.

Keywords: brake; clutch; drag loss; review

1. Introduction

Wet brakes and clutches (i.e., wet-running multi-plate brakes and clutches) are used across various sectors, including, but not limited to, automotive, maritime, agricultural, and industrial applications. In the automotive sector, famous applications include automatic transmissions, dual-clutch transmissions, limited-slip differentials, transfer cases, or torque vectoring systems. Extensive discussions currently focus on using wet brakes as in-drive brakes for electric vehicles. During the engaged state, torque and speed are transmitted based on friction. The torque to be transmitted can be flexibly adjusted, even during operation. The engagement and disengagement can be performed under differential speed. During the disengaged state and under the differential speed of the driving and driven shaft, the shearing of the fluid in the sub-millimeter gaps between the plates causes drag losses, which are typically converted into heat. The increased temperature, in turn, may affect the wear behavior of other machine elements and the aging of the oil [1]. The drag torque of wet brakes and clutches may affect a drivetrain's functionality; in the case of a dual-clutch transmission, the drag torque can affect the synchronization process [2]. Additionally, drag losses can account for a considerable share of the overall drivetrain losses. The total brakes' and clutches' drag losses can account for up to 46% of the total losses of an automatic transmission with six wet-type shifting elements, depending on the operating conditions such as current gear, torque, speed, or oil temperature [3]. Also, in the case of a dual-clutch transmission, the wet clutches' drag losses dominate the total losses [4]. The clutch-related losses can account for up to 40% of the total losses in specific operating conditions [5]. Due to the parasitic drag losses of wet brakes and clutches, research has also been conducted on alternative shifting element concepts. Replacing shifting elements of the multi-plate design,



Received: 3 December 2024

Revised: 21 December 2024

Accepted: 5 January 2025

Published: 10 January 2025

Citation: Pointner-Gabriel, L.; Voelkel, K.; Stahl, K. Drag Losses of Wet Brakes and Clutches—A Scoping Review. *Lubricants* **2025**, *13*, 27. <https://doi.org/10.3390/lubricants13010027>

Copyright: © 2025 by the authors. Licensee MDPI, Basel, Switzerland. This article is an open access article distributed under the terms and conditions of the Creative Commons Attribution (CC BY) license (<https://creativecommons.org/licenses/by/4.0/>).

e.g., by a combined cone and dog clutch [6] or band brake [7], can significantly reduce drag losses. However, the excellent shifting quality of wet brakes and clutches is still a significant advantage and hinders the mentioned designs from widespread implementation into drivetrains. Therefore, wet brakes and clutches are the shifting elements of choice in numerous applications. Research mainly, but not only, focuses on friction, thermal, damage, NVH (noise, vibration, harshness), and drag loss behavior. To the authors' knowledge, the current state of the art on drag loss behavior has not yet been summarized, which is relevant for developing efficient wet brake and clutch systems and identifying future research directions.

Therefore, the objective of this scoping review is to give a comprehensive overview of the existing knowledge of wet brakes' and clutches' drag loss behavior and identify future research directions. This review was conducted according to the PRISMA guideline [8] for transparent reporting of the document search and screening and the methods used. This review focuses on the disengaged state. Hence, research on the engagement and disengagement process and the engaged state was not considered. The review is limited to the integral effects of design and operating parameters on the drag loss behavior and methods for determining the drag losses. In-depth knowledge of local flow characteristics is not part of this review. From here on, only the term *wet clutch* will be used for good readability of this paper.

2. Fundamentals

Figure 1 shows a schematic representation of a wet clutch in the disengaged state. The clearances (i.e., distances between adjacent plates) are shown enlarged for visualization purposes. For real applications, clearances in the range of a few tenths of a millimeter are typical [1,9,10]. The main components are the inner and outer carrier, separator and friction plates, reaction ring, and piston. In Figure 1, the separator plates are the inner plates, and the friction plates are the outer plates. The inner and outer plates are alternately arranged and can—in the case of not being forced to distance—axially move within the set total clearance. If only one of the carriers rotates, it is referred to as the brake operation mode; if both carriers rotate, it is referred to as the clutch operation mode. The components' names are commonly used but may differ in some cases from those used in other research papers.

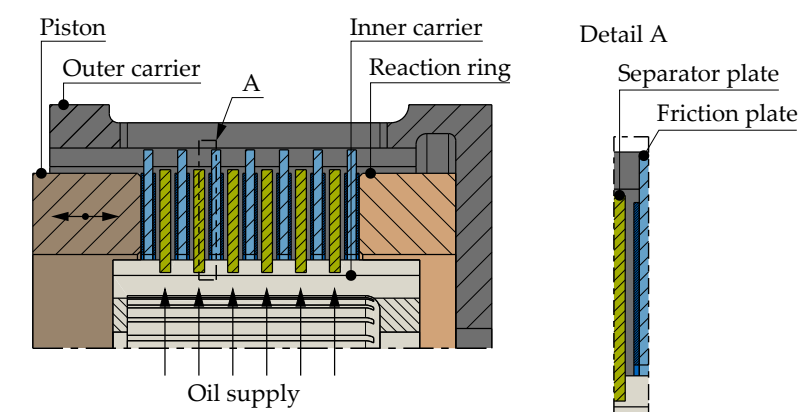


Figure 1. Schematic representation of an injection-lubricated clutch in disengaged state. Note: Clearances are shown enlarged for visualization purposes.

In order to better dissipate the heat generated during shifting, the clutch needs to be fluid-cooled. Depending on the requirements, injection or dip lubrication is typically applied. The oil is centrally supplied during injection lubrication (IL), representing active lubrication. In contrast, during dip lubrication (DL), the clutch components permanently dip into an oil sump of a specific level, representing passive lubrication. Injection lubrication

is typically used in applications with high cooling demands. In contrast, the low overall complexity is advantageous when using dip lubrication.

The flow in the gaps can be characterized as complex, wall-bounded, sub-millimeter shear flow [11]. Generally, the flow pattern prevailing in the gaps of adjacent plates is primarily shaped by the acting centrifugal and viscous forces and the surface tension [12]. Surface tension forces try to maintain the fluid as a continuous film, while centrifugal forces try to rupture it [13]. Strong wall effects are also acting [13]. In the case of the widely applied injection lubrication, the oil is continuously supplied with a specific flow rate. During low differential speeds and, thus, low centrifugal force acting on the oil, the radial flow velocity decelerates towards the outer radius according to the law of continuity [12]. Hence, the gaps are fully filled, which represents a single-phase flow. Generally, the flow can be described as a superimposition of a circumferential Couette-like shear flow, radial Poiseuille-like pressure flow, and radial inertia flow resulting from centrifugal forces [14]. The radial pressure flow dominates in the low differential speed region, driven by the continuous oil supply and corresponding feeding pressure [15]. Figure 2 shows the flow conditions in the gap during low differential speeds.

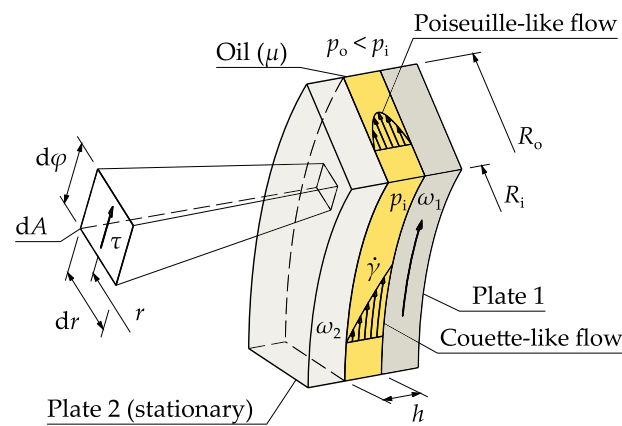


Figure 2. Flow conditions in the gap during low differential speeds inspired by Ref. [16]. Figure adapted with permission (Shaker).

The circumferential Couette-like flow causes a characteristic shear stress distribution on the plates' surfaces, significantly influenced by their design and operating parameters. The integral shear stress represents a circumferential force and, in turn, the drag torque when multiplied by the plate radius. Therefore, the drag torque is an integral parameter of the complex flow conditions in the gap and can be directly influenced by changing the flow of any kind. The drag torque T can be derived from the circumferential shear stress τ based on Newton's law of viscosity according to Equation (1). A fully oil-filled gap of constant clearance and a laminar and incompressible flow is assumed. Equation (2) finally shows that drag torque T depends on differential speed $\Delta\omega$, plate size $(R_o^4 - R_i^4)$, oil viscosity μ , and clearance h . [16]

$$dT = \tau \cdot dA \cdot r = \mu \cdot \dot{\gamma} \cdot dA \cdot r \quad (1)$$

$$T = \mu \frac{(\omega_1 - \omega_2)}{h} \int_0^{2\pi} \int_{R_i}^{R_o} r^3 dr d\varphi = \pi \mu \frac{\Delta\omega}{2h} \cdot (R_o^4 - R_i^4) \quad (2)$$

However, upon a certain differential speed, the then-dominant centrifugal force drives the oil outwards; the radial flow is hindered from decelerating following the law of continuity [12]. Consequently, air enters the gaps, and a two-phase flow (i.e., oil–air mixture) is present. The onset of air entering the gaps is generally referred to as aeration. In other words, aeration occurs when the theoretical feed rate of the clutch exceeds the supplied flow rate. The air content continuously increases with differential speed.

During dip lubrication and low differential speeds, the gaps are also fully filled with oil. However, in contrast to injection lubrication, the oil is continuously displaced from the gaps, starting from the inside with increasing differential speed and, thus, increasing centrifugal force. Hence, a two-phase flow is also present in the gaps. With increasing differential speed, the oil is continuously displaced from the gaps until the gaps are almost free of oil. [17]

It can be summarized that drag loss behavior is strongly dependent on the differential speed. Therefore, the drag loss behavior of wet clutches is typically described by the drag torque versus the differential speed. As shown in Figure 3, the drag torque first increases with increasing differential speed, according to Equation (2). After aeration or oil displacement, the drag torque can continue to increase degressively [17]. However, it then drops due to the decreasing effective viscosity of the oil–air mixture. The drag torque then stagnates at a low level and may re-increase abruptly due to speed-induced phenomena at high rotational speeds. The curve progression is significantly influenced by the clutch design and operating conditions [15]. For distinguishing purposes, the described drag torque curve is typically divided into phases, whereby different limits and notations of the phases are used. The classification used in Figure 3 (i.e., Phases 1, 2, and 3—introduced in Ref. [18]) is widely used and is therefore also used in this review paper. Phase 1 is often subdivided into Phases 1a and 1b [10,19,20]. Other research teams divide the phases into low-, mid-, and high-speed zones [1,21,22]. The characteristic drag torque curve occurs for injection and dip lubrication, though the flow in the gaps develops differently [17].

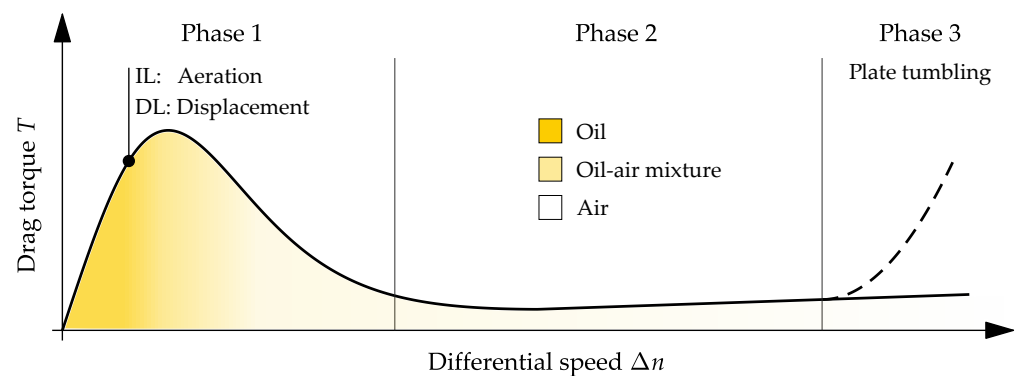


Figure 3. Characteristic drag torque curve and its classification inspired by Ref. [23]. Figure adapted with permission by CC BY 4.0 (Springer). Note: DL, dip lubrication; IL, injection lubrication.

The sudden re-increase in drag torque is caused by mechanical contact of adjacent plates, which, in turn, is caused by instabilities of the rotating plates at high rotational speeds. This phenomenon is called plate tumbling or wobbling and comes with high-frequency impacts. Plate tumbling is a superposition of multiple harmonic motions, each characterized by a different frequency. With increasing rotational speed, the dominant frequency increases, which, in turn, causes an increase in drag torque due to higher accumulated sliding friction per time unit. [24]

Another explanation approach sees the decreasing local static pressure at the oil outlet as responsible for the increased drag torque at high rotational speeds. When the local static pressure drops beyond a specific value, the plates are pulled closer together, which causes generally smaller clearances. Using spacing elements that prevent the plates from moving avoids a re-increase in drag torque. [25]

3. Methodology

The scoping review was conducted according to the PRISMA guideline [8]. The protocol for this scoping review was registered on the Open Science Framework (OSF) and can be accessed at <https://doi.org/10.17605/OSF.IO/PN48J> (accessed on 2 December 2024).

3.1. Document Search and Screening

After some iterations and discussion among the authors, the final search query formulation was defined as visualized in Figure 4. The keywords used to compose the string are divided into two categories. The first category concerns the components of brakes and clutches in general, and the second category concerns their drag losses.

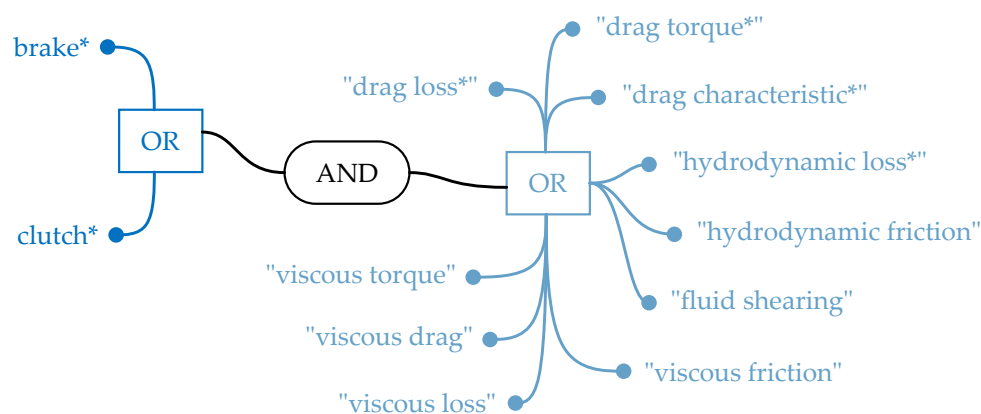


Figure 4. Visualization of final search query input into Scopus and Web of Science databases.

The systematic search was conducted on 25 October 2024 using the Scopus [26] and Web of Science [27] databases. It was searched within the title, abstract, and keywords. The considered time span was not limited. Additionally, a manual search was conducted using both databases and also the THEMIS [28] database. The THEMIS database is hosted by the Research Association for Drive Technology e. V. (FVA), located in Germany. The findings of the research projects organized by FVA represent an essential contribution to the existing body of literature and need to be considered in this review. However, the final reports of the research projects are only accessible to a limited extent. The PRISMA flow diagram is shown in Figure 5.

The search query showed 349 results on Scopus and 178 on Web of Science. Additionally, 14 relevant documents were identified via manual database search. The documents were filtered by language; only the English and German languages were considered. Duplicates were identified and excluded, narrowing the body of literature to 345 documents. The documents were manually screened in three steps, i.e., title, abstract, and full-text screening. The screening process was performed using the raiyan [29] web app. Title and abstract screening narrowed the body of literature to 113 documents. The remaining documents were read and screened in line with the exclusion criteria listed in Table 1, further narrowing the body of literature to 93 documents. In case documents substantially overlapped, only the most comprehensive version was included. The bibliography also includes 15 supplementary references cited mainly in Sections 1 and 3.

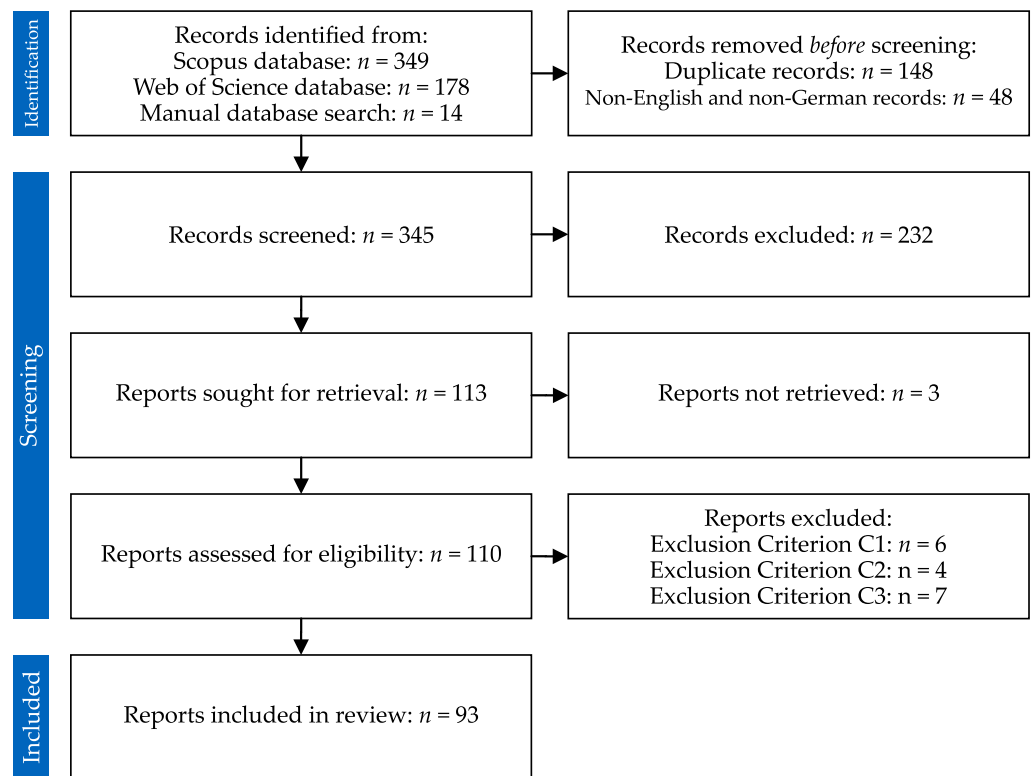


Figure 5. PRISMA flow diagram, adapted with permission by CC BY 4.0 (PRISMA 2020).

Table 1. Criteria used for exclusion of documents based on manual full-text screening.

Exclusion Criteria
C1: Document falls outside the review's scope
C2: Document with incomplete reporting of key information
C3: Document shows substantial similarity to other records

3.2. Framework for Data Extraction and Synthesis of Results

A framework was defined after discussion among the authors for targeted data extraction. The framework is reported in Table 2.

Table 2. Framework for data extraction.

Groups	Features
Metadata	Year and country of publication and type and language of document
General data	Research method, field of application, type of lubrication, and investigated design and operating parameters
Experimental testing	Test rig concept, test procedure, flow visualization and capturing technique, and other specifics
Analytical calculation	Validity range, flow modeling approach, validation, drag torque equation, and other specifics
Numerical calculation	Objective, flow modeling, flow domain, simplifications, boundary conditions, validation, mesh size, software, and other specifics
Data-driven calculation	Scope of application, input and output, algorithm, model performance, dataset structure, and other specifics

The results were summarized in narrative, tabular, and visual formats. Tree maps, pie charts, and histograms were created to illustrate document distributions per defined features.

4. Results

4.1. Overview

Figure 6 shows the number of documents published over the years. The visualization shows that the drag losses of wet clutches have been the subject of research since the 1970s until today. However, most of the documents were published in the last 15 years, with a peak in 2019. The figure indicates a growing interest in this field of research.

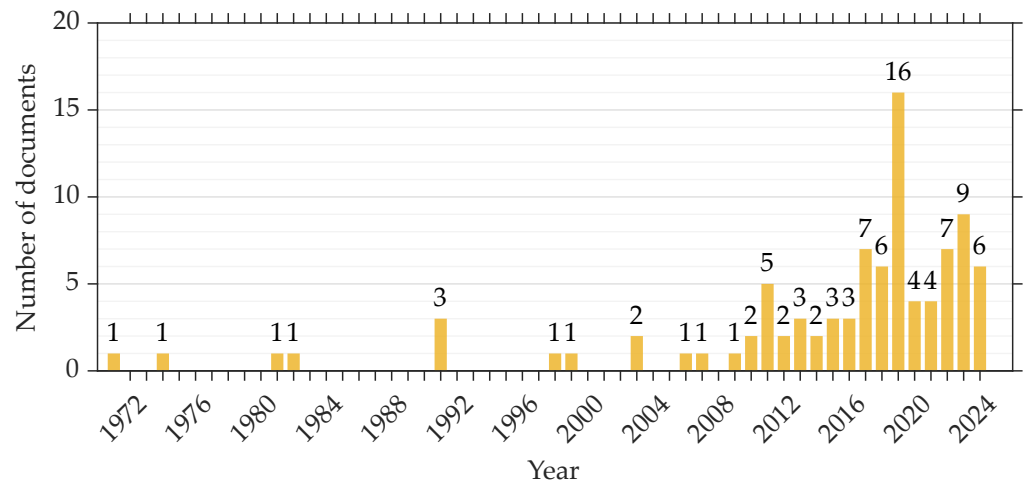


Figure 6. Distribution of documents per year.

Figure 7 visualizes the distribution of the documents per country and document type. The research was mainly driven by German, Chinese, US, and Japanese research teams; see Figure 7a. Most documents are published as articles and conference papers. FVA reports represent only a minor share of the document set; see Figure 7b. The analysis showed that 84% of documents are written in English and 16% in German.

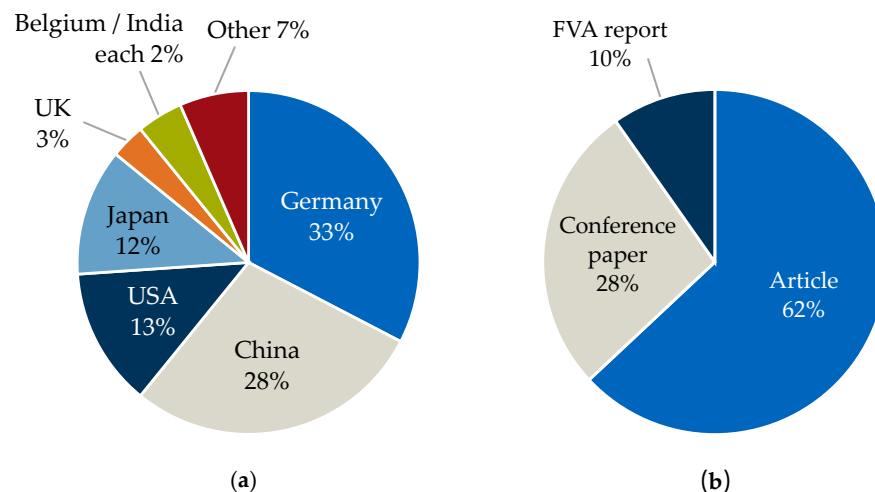


Figure 7. Distribution of documents (a) per country; (b) per document type.

Figure 8 shows the tree maps of the reviewed documents for the applied research method, field of application, lubrication type, and groove design. Since categorization does not apply to the entire document set, the tree maps are based on specific sub-sets whose sizes are given in the figure caption. Since some documents apply to multiple categories, relative values are considered.

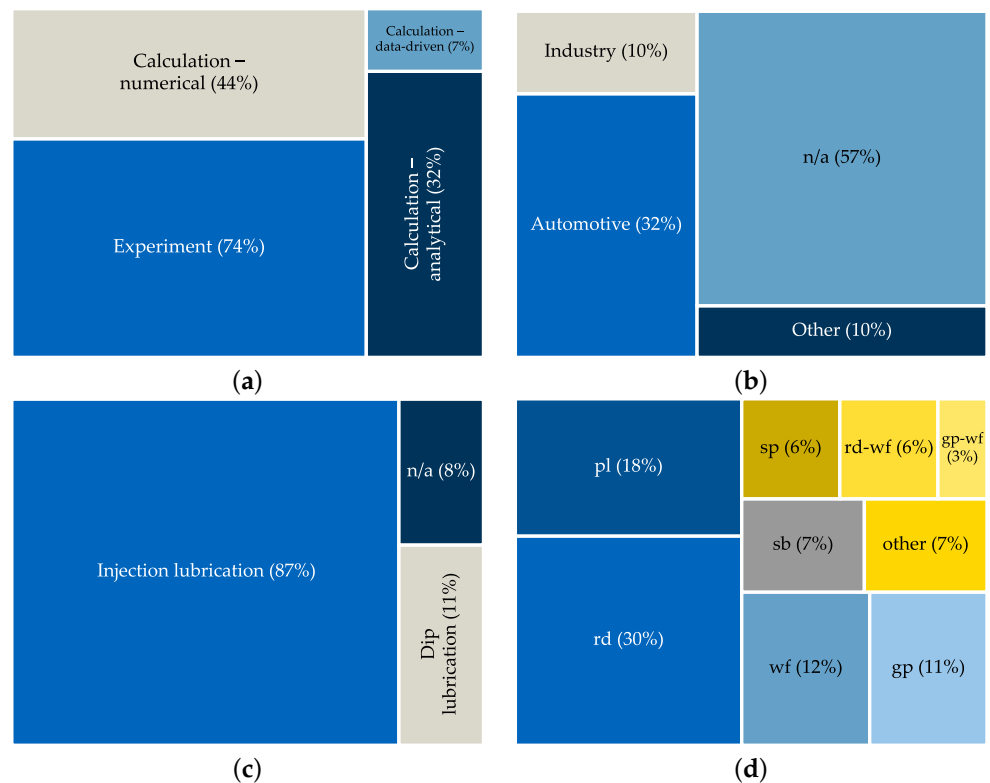


Figure 8. Distribution of documents (a) per research method (for 93 documents); (b) per field of application (for 93 documents); (c) per lubrication type (for 93 documents); (d) per groove design (for 72 documents). Note: gp, group-parallel; pl, plain; rd, radial; sb, sunburst; sp, spiral; wf, waffle.

The applied research methods are balanced between experiment and calculation; see Figure 8a. Experimental studies were performed to investigate the integral drag losses and flow characteristics and validate the calculation models. Calculations in the context of wet clutches' drag losses are based on numerical, analytical, and data-driven modeling approaches. In detail, the analysis revealed that 74% of the documents can be associated with experimental research, 45% with numerical, 33% with analytical, and only 7% with data-driven calculation. It can be seen in Figure 8b that drag loss research has been mainly driven by the automotive sector, followed by the industry sector, and others such as maritime or aviation. Furthermore, the analysis revealed that most studies used injection lubrication; only 11% used dip lubrication; see Figure 8c. Figure 8d shows the distribution of groove designs investigated by experiment or simulation. The groove designs are schematically shown in Figure A1 of Appendix A. It can be clearly seen that most of the studies focused on the radial, waffle, or group-parallel groove designs. A considerable share of studies used plain (i.e., non-grooved) plates. Superimposed groove designs were also widely used, such as radial and waffle or group-parallel and waffle. If the friction lining is not continuous and consists of individual pads attached to the core plate, this configuration is known as multi-segmented friction lining, as exemplified in Ref. [9]. The gaps between the pads form grooves, resulting in a radial or group-parallel design. Typically, grooves are added to the pads [9,10]. Modifications of the base groove designs are sometimes applied for optimization reasons. For example, radial grooves can be purely radial but also inclined [10,15,30,31] or modified [25,32–36]. Figure 9 gives an overview of the parameters investigated to date.

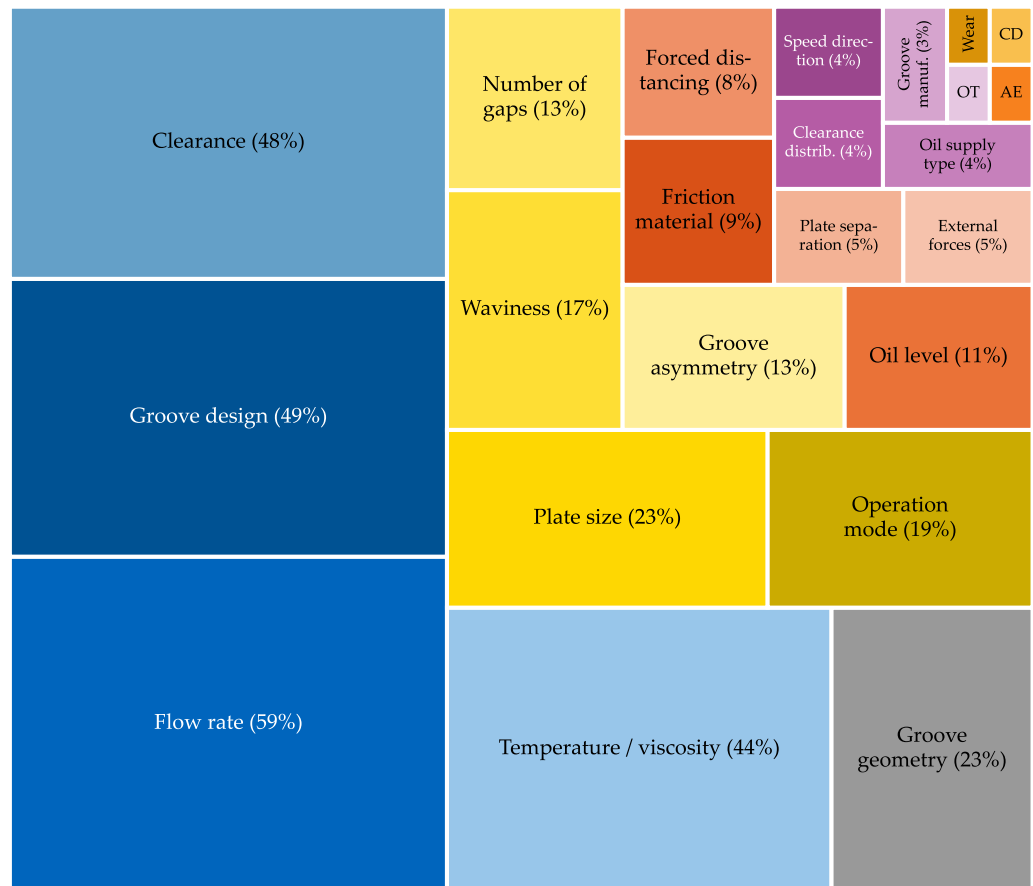


Figure 9. Distribution of documents per parameter investigated (for 75 documents). Note: AE, air entrainment; CD, carrier design; OT, oil type; each 1%.

Most of the studies focused on the parameters of flow rate, groove design, clearance, and oil temperature or viscosity. In contrast, parameters like air entrainment, wear, carrier design, or oil type have rarely been the subject of investigations to date. The resulting parameter effects on drag loss behavior are discussed in Section 4.2.

Figure 10 shows the distribution of the documents per mean plate diameter, maximum differential speed, and minimum and maximum oil temperature.

It can be clearly seen in Figure 10a that drag loss research has been mainly conducted for clutch plates with a mean diameter in the range of 100 mm and 250 mm. The maximum mean plate diameter investigated so far is 515 mm [37]. Additionally, the analysis revealed that investigations concentrated on moderate maximum differential speeds; see Figure 10b. Only approx. 10% of the studies have investigated the high differential speed range of over 10,000 rpm. Furthermore, the analysis showed that the influence of sub-zero oil temperature and, consequently, high oil viscosity have been investigated only in a few studies; see Figure 10c. The maximum oil temperatures ranged between 100 °C and 125 °C.

Table 3. Cont.

Numbering	Reference	Research Method	Type of Lubrication	Torque Re-Increase	Plate Size	Number of Gaps	Groove Design	Groove Geometry	Groove Asymmetry	Waviness	Material	Groove Manufacturing	Carrier Design	Operation Mode	Clearance	Clearance Distribution	Plate Separation	Flow Rate	Oil Supply Type	Oil Level	Temperature/Viscosity	Oil Type	Air Entrainment	Forced Distancing	External Forces	Wear	Speed Direction
25	[55]	EX/CA	IL		•									•							•						
26	[56]	EX/CA	IL		•										•						•						
27	[32]	EX/CA	IL				•																				
28	[57]	CA	IL					•																			
29	[58]	CA	IL					•								•											
30	[59]	EX/CA	IL	×	•	•	•			•	•		•	•	•						•					•	•
31	[33]	EX/CA	IL				•																				
32	[24]	EX	IL	×		•								•	•												
33	[25]	EX/CA	IL	×			•								•						•						
34	[60]	EX/CA	IL	×											•									•			
35	[61]	EX/CA	IL				•																	•			
36	[62]	EX/CA	IL				•	•											•								
37	[63]	EX/CA	IL	×														•		•							
38	[15]	EX/CA	IL				•	•	•						•						•						
39	[64]	EX	IL	×			•														•						
40	[65]	EX/CA	IL				•	•							•						•			•			
41	[66]	EX/CA	IL				•		•						•						•						
42	[67]	EX/CA	IL				•							•	•						•						
43	[68]	EX/CA	DL																		•						
44	[69]	EX/CA	IL												•						•						
45	[70]	EX/CA	IL												•						•						
46	[71]	EX/CA	DL																		•						
47	[14]	EX/CA	IL				•	•	•						•						•						
48	[72]	EX/CA	IL				•														•						
49	[73]	EX/CA	IL								•										•						
50	[22]	EX/CA	IL																		•						
51	[74]	EX/CA	IL				•	•		•											•						
52	[75]	EX/CA	IL												•						•						
53	[76]	EX/CA	IL	×																	•						
54	[77]	EX/CA	IL				•							•							•						
55	[78]	CA	IL											•							•						
56	[79]	CA	IL																		•						
57	[80]	EX/CA	IL				•											•									
58	[36]	EX/CA	IL					•													•						
59	[81]	EX	IL												•						•						
60	[82]	CA	IL					•							•						•						
61	[19]	EX	DL		•	•	•	•							•						•						
62	[83]	EX/CA	IL/DL		•	•	•	•						•	•						•	•					
63	[35]	CA	IL				•														•						
64	[84]	EX/CA	IL												•						•						
65	[85]	EX	IL																		•						
66	[21]	EX/CA	IL												•						•			•			
67	[17]	EX	DL																		•						
68	[86]	CA	IL					•													•						
69	[34]	EX/CA	IL				•		•												•						
70	[87]	CA	IL					•													•						
71	[88]	EX/CA	IL/DL		•	•	•	•	•	•				•	•	•	•	•	•	•	•		•	•	•		
72	[10]	EX	IL/DL		•		•		•	•					•						•	•	•				
73	[89]	CA	DL		•	•	•								•						•						
74	[20]	EX	IL		•	•				•					•						•						
75	[90]	EX/CA	IL	×			•																	•	•		

4.2.1. Influence of Plate Size, Number of Gaps, Waviness, and Carrier Design

Increasing the plate size (i.e., diameter) significantly increases drag losses; see Equation (2). This was confirmed by all studies reviewed. In theory, the drag torque increases to the fourth power of the diameter. Small-diameter plates proved advantageous concerning plate tumbling [59]. However, it is assumed that design parameters, such as plate thickness and, thus, mass moment of inertia and stiffness, play a role, too [59]. Increasing the number of plates composing the clutch pack and, thus, the number of friction interfaces or gaps was found to increase the drag losses nearly proportional [9,41]. However, if plates do not adequately separate or even stay in contact, the drag torque is determined mainly by these pairs of plates [41]. The gap-specific losses at high gap numbers were found to be somewhat lower than with low gap numbers, which contradicts the assumption that the tendency towards non-uniform clearance distribution and, thus,

increased drag losses increases with the number of gaps [9]. For high rotational speeds, reducing the number of plates delays the drag torque re-increase [24]. However, it was also found that the effect of the number of gaps on the drag loss behavior at high rotational speeds can differ between clutch systems [59]. Waved plates are typically used to realize comfortable shifting and reduce drag losses due to better plate separation [18]. The studies reviewed largely confirmed the loss-reducing effect in Phases 1 and 2. In Phase 3, however, the drag torque increases with increasing wave height [18].

Increasing the cross-section of the outer carrier's oil outlet holes was found to significantly reduce drag losses, particularly in Phase 1. This effect is likely due to the larger cross-section allowing the oil to leave the gaps more freely. However, the loss-reducing effect was not observed in Phase 2, suggesting that even with a smaller cross-section, all of the oil can be efficiently conveyed outwards. [59]

4.2.2. Influence of Groove Design, Asymmetry, Geometry, and Manufacturing

Creating a universal ranking of categorical groove designs for minimal drag losses is not possible. Specific groove features can be beneficial in the low-speed region but disadvantageous in the high-speed region. Therefore, different base groove designs may be superimposed to combine advantages [14]. Additionally, as discussed later in this section, the design of the groove profile significantly influences the drag losses. Therefore, the results of the categoric groove design are not entirely consistent. In Ref. [18], the group-parallel groove design was found to cause higher drag losses on average than the waffle groove design. For paper-based friction linings, multi-segmentation of the lining was proved to be advantageous, with relatively small differences between the various forms of segmentation [9]. For sinter-metallic friction linings, the waffle groove design and a geometrically similar sunburst groove design were reported to be at a low drag loss level without significant differences, while the investigated spiral groove design showed significantly higher losses [9]. In contrast, significant differences between the waffle and sunburst groove designs are reported in Ref. [19]. The spiral and sunburst groove designs cause significantly higher drag losses than the radial and group-parallel groove designs, particularly at high speeds and low oil viscosities [39]. This is broadly consistent with the findings described in Ref. [41]; low drag torques were achieved with the radial and waffle groove designs, slightly higher drag torques with the sunburst groove design, and relatively high drag torques with the spiral groove design. In Ref. [72], the sunburst groove design was reported to cause higher drag losses than the radial groove design. Often, asymmetric groove designs such as the radial with inclined grooves or a spiral are used to improve the drag loss behavior by increasing the conveying capacity. Hence, an inclination of the grooves against the direction of rotation increases the conveying rate analogously to radial pumps in the case of injection lubrication. Consequently, aeration sets in at lower differential speeds [14,15]. The drag torque level tends to decrease with increasing groove angle, particularly at low differential speeds [14,15]. However, interactions between groove angle and clearance were reported, i.e., increased drag losses can occur in the two-phase region even at higher inclination angles in the case of a small clearance [15]. It was found that the optimal groove angle reduces with increasing differential speed [14]. In the case of the spiral groove design, a loss-reducing effect can be reached with positive spiral grooves, which support the outward flow [9,66]. In contrast, in the case of dip lubrication, an inclination of the grooves against the direction of rotation causes a blocking behavior, which results in reduced drag losses [10]. Improving the groove geometry or profile offers the potential for drag loss reduction. An optimized groove design can not only reduce the viscous drag losses but also enhance the critical rotational speed for sudden re-increase in drag torque and reduce drag losses at high rotational speeds through reduced impact

frequency and intensity [90]. Several studies used the comparable simple radial groove design to investigate the effects of groove geometry on drag loss behavior. It was reported that increasing the groove width or depth causes a decrease in drag torque due to increasing total groove cross-sectional area and, consequently, higher conveying rate [31,50,62,65,74]. However, in contrast, the torque-reducing effect when increasing depth was not reported in Ref. [31]. With an increasing number of radial grooves, a significant reduction in drag torque [15,31,58,82] and faster aeration may be achieved [15,82]. However, introducing more grooves reduces the frictional contact surface. Given a constant frictional contact surface, it is preferable to use a high number of thin grooves [15]. Keeping the groove cross-sectional area and number of grooves constant while varying groove depth and width only showed minor differences in the drag torque [15,82]. Modifying the inlet and outlet of the radial grooves was found to result in significant drag torque reduction [36].

In paper-based friction linings, the grooves are typically milled, punched, or embossed, with each manufacturing process showing characteristic deviations from the nominal geometry. It was reported that the groove manufacturing process influences drag losses. Milled grooves are characterized by upwardly curving edges and almost vertical lateral groove boundaries. In contrast, punched grooves show rounded edges. Embossed grooves additionally show round transitions in the groove base. Generally, sharp-edged groove profiles and burrs, which often occur with milled grooves, are to be avoided. Therefore, punched grooves with more rounded edges result in lower maximum drag torques. Embossed grooves cause even lower drag torque, as they have the largest edge radii. However, sharp-edged groove profiles cause faster aeration due to the premature rupture of the oil film in Phase 1. For applications in the high differential speed range, milled grooves should be avoided due to the expected high drag losses. [18]

4.2.3. Influence of Material and Wear

Due to their excellent friction, damage, and wear behavior, paper-based, carbon, and sinter-metallic friction linings are typically used in wet clutch applications. It has been shown that the wettability of the friction plates (i.e., the contact angle between oil and solid surface) significantly influences the drag torque [49]. A small contact angle means the oil film can be maintained up to higher differential speeds, resulting in a higher drag torque [31]. In the context of drag loss research, non-standard materials such as PTFE and aluminum were investigated [31,49,73]. However, comparing practice-oriented friction materials such as paper and sintered bronze revealed insignificant differences [39]. Another study rated the influence of the friction material as extremely small [18]. With paper-based friction lining, plate tumbling occurred at higher differential speeds compared to sinter-metallic friction lining [59].

The drag loss behavior of new and used plates was determined and compared to investigate the wear effect. Topographic measurements of the used plates showed considerable smoothing of the friction plates and marks in the circumferential direction on the separator plates. The reduced thickness of the used plates was compensated in the clearance configuration of the new plates to avoid a clearance-related reduction in drag torque. Generally, wear (i.e., smoothing and marks) was found to increase drag losses, particularly in Phases 2 and 3. It is assumed that higher adhesive forces on the smoothed surface of the friction plates or the wear-related reduction in groove volume may be the primary cause. [59]

4.2.4. Influence of Oil Supply Type, Flow Rate, and Oil Level

Different oil supply methods, such as internal and external injection lubrication and dip lubrication, were applied during drag loss investigation. A comparison of internal

injection and dip lubrication of moderate injection flow rate or oil level revealed that the latter has significantly lower drag losses [10]. However, dip lubrication provides limited cooling performance since oil displacement sets in already at low differential speeds [10]. In the case of external injection lubrication, it is more difficult to supply oil to the gaps against the clutch's conveying, which is why this lubrication type results in low drag losses [62]. All reviewed documents report that an increase in injection flow rate increases drag torque due to the gaps being filled up to higher differential speeds. Consequently, aeration occurs at a higher differential speed. However, it was observed that drag losses do not increase further beyond a specific injection flow rate since the clutch's feed capacity is utilized at some point, and the supplied oil flows off axially [88]. It was also observed that a higher injection flow rate delays the sudden re-increase in drag torque to higher rotational speeds [76]. However, once the re-increase occurs, a higher flow rate causes a high amplitude and growth rate of drag torque [76]. All studies concluded that increasing the oil level leads to higher drag losses. However, it was also reported that the effects of the oil level have a minor impact, which is why this parameter offers only limited potential for systematic drag loss reduction [10]. Generally, a higher oil level requires higher centrifugal forces to displace the oil and thus extends the oil displacement process [17].

4.2.5. Influence of Oil Type, Temperature/Viscosity, and Air Entrainment

It was found that slightly reducing the base oil viscosity and improving the viscosity index through additives can lead to a considerable drag loss reduction. However, the primary cause for the significant reduction could not be conclusively clarified. Surface tension or another unknown parameter may potentially affect the results. [9]

It is common knowledge that drag torque depends on oil viscosity; see Equation (2). The oil viscosity is dependent on temperature, which is why existing knowledge of temperature and viscosity effects are discussed collectively. A high oil temperature, and, thus, low viscosity, is advantageous for reducing drag losses.

It was found that in the case of dip lubrication, air is entrained into the oil due to the continuous dipping of the plates [19]. Additionally, in the case of injection lubrication, air entrainment is caused by the aeration process. This means that the re-supplied oil may be air-entrained, too. Consequently, an oil–air mixture may be present in the gaps even before the onset of aeration.

Generally, the drag losses decrease with increasing air content. However, the underlying phenomenon is differential-speed-dependent. In Phase 1a and, thus, in the phase of the completely filled gap, the drag torque decreases with increasing air content due to the reduced viscosity of the oil–air mixture. After aeration onset, an oil–air mixture forms in the gap anyway. Therefore, the influence of the air content present in the supplied oil–air mixture decreases in Phase 1b. In Phase 2, there is no longer any influence of air since the aeration process dominates the composition of the oil–air mixture. [88]

4.2.6. Influence of Clearance

It is common knowledge that drag torque depends on clearance; see Equation (2). All reviewed documents report that an increase in clearance leads to lower drag losses. This is due to the reduced velocity gradient perpendicular to the shear direction or reduced shear rate. However, increasing the clearance reduces hydrodynamic drag losses, although a sudden re-increase at high rotational speed is more likely [59].

4.2.7. Influence of Plate Separation, Clearance Distribution, and Forced Distancing

Plate separation, clearance distribution, and forced distancing are closely linked and are therefore discussed collectively. Generally, drag losses can be reduced by ensuring reliable, rapid, and uniform plate separation [80]. However, it is commonly known that

the plates continuously move in real-world applications within the set total clearance, which affects uniform plate distribution. Plate separation can be supported by mechanical restoring forces provided by waved plates or spacing elements. Also, hydrodynamic axial forces caused by the oil flow can be utilized to separate plates [80]. These forces can be significantly improved by an optimized groove design [58,80]. Notably, radially closed or half-moon-shaped grooves support plate separation [80]. The micro geometry of the groove edges, which largely depends on the applied manufacturing process, was also found to significantly influence the pressure distribution [80]. An asymmetrical groove edge design was found to cause higher axial forces [80]. Also, it was found that axial forces acting on the plates decrease with increasing differential speed due to decreasing oil volume fraction inside the gaps [58,80]. Plate separation is mainly driven by the applied differential speed, which means that the set total clearance is typically only utilized in the higher differential speed range [88]. The plates may remain in contact at low differential speeds, making waved plates advantageous for applications characterized by low differential speeds [88]. Minimizing drag losses is closely tied to achieving a uniform distribution of the set total clearance to the gaps [41]. However, a uniform clearance distribution can be practically reached only by using spacing elements such as wave springs, which mechanically provide restoring forces. It was found that forced plate distancing also avoids the influence of external forces on the drag loss behavior [20]. It was also found that ensuring constant plate positions can prevent drag torque from re-increasing at high rotational speeds [64]. Simulations showed that a non-uniform clearance distribution causes different flow states in the gaps [79]. Consequently, different pressure conditions between two sides of the plates may be the primary cause of axial plate oscillations [79].

4.2.8. Influence of Operation Mode and Speed Direction

The operation mode depends on the application. If only one of the carriers rotates, it is referred to as the brake operation mode; if both carriers rotate, it is referred to as the clutch operation mode. For the latter, the co- and counter-directional rotation of the carriers must be distinguished. Generally, the reported effects of the operation mode on the drag loss behavior differ. On the one hand, it was reported that in brake operation mode, rotating friction plates cause a higher drag torque level than rotating separator plates [41]. On the other hand, it was found that rotating friction plates are usually, but not generally, advantageous [9]. Furthermore, it was stated that the counter-directional rotational state exhibits the highest, while the co-directional rotational state exhibits the lowest, overall drag torque [1]. Some studies observed hysteresis effects, which means that aeration [30] or plate tumbling [59] depends on the direction of speed change. For increasing differential speed, aeration occurred at higher speeds than when flooding (i.e., the reverse of aeration for decreasing differential speed) [30]. A similar behavior was observed for plate tumbling, which only stopped when the differential speed was significantly reduced below the value at which it had started [59].

4.2.9. Influence of External Forces

External forces can be introduced, e.g., through vehicle movements, a non-horizontal installation, or vibrations. The review revealed that, to date, only the effect of constant external forces has been investigated; the effect of dynamic external forces has yet to be investigated. A recently published study [20] found that external forces acting on the plates influence their separation and distribution. This, in turn, affects the drag loss behavior. The investigations showed that even under the 15° inclination, the plates separate, and the drag torque curve shows characteristics similar to wet clutches operated without external

forces applied. However, with increasing external forces, drag losses increase due to decreasing clearances.

4.2.10. Design Trade-Offs

As described above, numerous parameters offer the potential to reduce drag losses. However, different aspects must be considered holistically during clutch development. On the one hand, increasing the clearance reduces the drag losses. On the other hand, it simultaneously leads to a longer shifting time [56], less robust engagement control [61], a higher likelihood of torque jump-up at high rotational speeds [60], and consumes more axial installation space. Reducing the injection flow rate or level reduces the drag losses but may negatively affect the cooling performance or even cause damage in the worst case [91]. Increasing the groove area can reduce drag losses and improve cooling performance, but it also reduces the frictional contact surface, potentially compromising the material's structural integrity [61]. Also, reducing the oil viscosity reduces the drag losses but may affect the friction behavior during the engaged state and the lubrication of other drivetrain components. Reducing the number of plates and, consequently, the friction interfaces or gaps in the disengaged state, respectively, reduces the drag losses but also reduces the transmittable friction torque. For a low-loss clutch system, it is usually best to aim for the smallest possible total frictional contact surface [9]. Spacing elements can minimize the drag losses but require installation space [85] and cause higher costs.

It can be concluded that clutch design must be carried out holistically. This means that drag loss, friction, thermal, and damage behavior must be considered simultaneously, and any changes made to one aspect should be evaluated in the context of its impact on the entire system.

4.3. Methods for Experimental Investigation of Drag Losses

4.3.1. Measurement of Integral Drag Torque

Integral drag torque refers to the drag torque of the entire system, while local drag torque pertains to the drag torque generated in specific sections. This review revealed that two different test rig concepts, namely the model-level and component-level test rig concept, are typically applied to measure the integral drag torque of a single gap or an entire clutch system; see Figure 11a. Further, this review revealed that different test procedures are typically applied to determine the integral drag torque curve; see Figure 11b. The test procedures are discussed below. It should be noted that a considerable share of documents does not clearly report the applied test procedure.

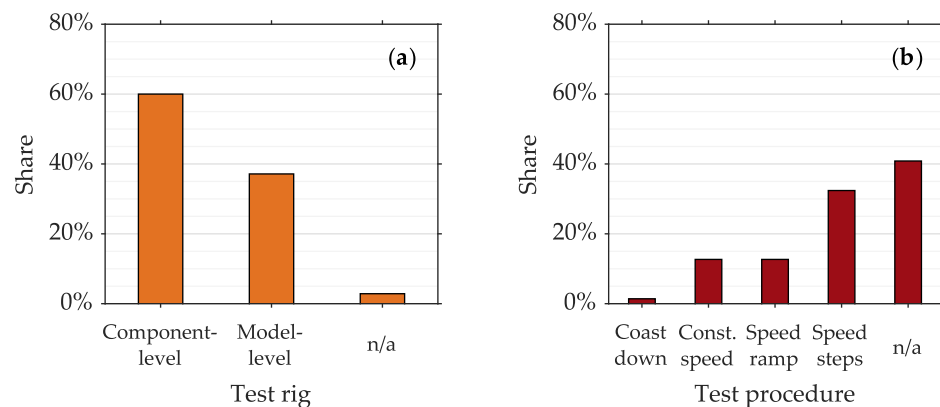


Figure 11. Distribution of documents (a) per test rig concept (for 71 documents); (b) per test procedure (for 72 documents).

Model-level test rigs were used in the studies of Refs. [15,31,34,92], e.g., and component-level test rigs of Refs. [1,9,19,39,42]. Figure 12 schematically shows the model-level and component-level test rig concepts.

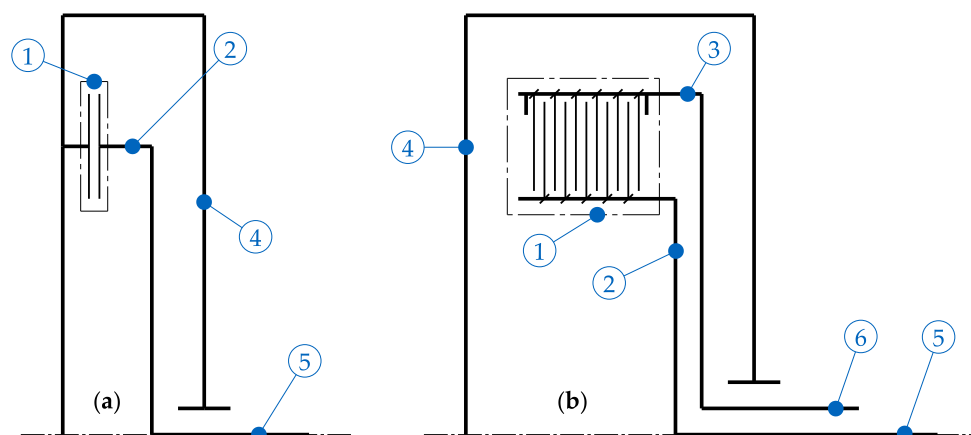


Figure 12. Test rig concepts: (a) model-level test rig; (b) component-level test rig. Note: (1) clutch plates; (2) inner carrier; (3) outer carrier; (4) housing; (5) drive inner carrier; (6) drive outer carrier.

Model-level test rigs are suitable for investigations based on a reduced clutch system, meaning only one or two gaps are typically considered. The clearance is typically constant, which helps to avoid influences from changing plate positions. Hence, model-level test rigs are particularly suitable, e.g., for in-depth investigations focusing on the groove design effects and validation of calculation models. In contrast, component-level test rigs allow investigations based on the entire clutch system. Hence, component-level test rigs enable, for instance, investigating the effects of plate movements or carrier design on drag loss behavior.

The drag torque can be measured directly via a torque measuring shaft (i.e., strain gauges [9] or optical-electronic light method [1]) or indirectly via a load cell and lever [15]. For investigation under real-world operating conditions of external forces, test rigs were inclined [20,43]. Several studies included a run-in of the clutch plates to guarantee a stabilized behavior [1,39,42,70]. This ensures that results are not affected by changes in surface conditions that generally occur after brief usage [42]. It was shown that the oil temperature at the clutch pack outlet and the plate temperature initially rise due to the dissipation of the drag torque but then reach a steady-state temperature level [45]. Accordingly, the drag torque decreases due to the viscosity dependency. Hence, performing a pre-run for tempering the clutch components and guaranteeing stabilized conditions is essential for determining the steady drag torque.

The drag torque is typically measured with respect to the differential speed. The increasing, decreasing, or both speed paths are investigated depending on the research objective. Figure 13 shows two different types of test procedures widely applied.

Increasing the differential speed with a specific angular acceleration (i.e., speed ramp), as shown in Figure 13a, allows time-efficient measurement of the drag torque curve within several minutes, as can be seen from Refs. [9,16,41]. However, it needs to be considered that the drag torque is not measured under steady conditions. Keeping the angular acceleration at a low value minimizes this influence. Experiments showed that a quasi-steady behavior can be obtained in the case of moderate angular acceleration of 10 rpm/s, and the measurements yield results equivalent to steady operating conditions [15]. However, depending on the torque measurement method and sensor arrangement, the measured torque may also include the acceleration torque caused by the inertia of the accelerated

clutch components [23]. The acceleration torque can be determined through a baseline measurement and considered during the final test evaluation.

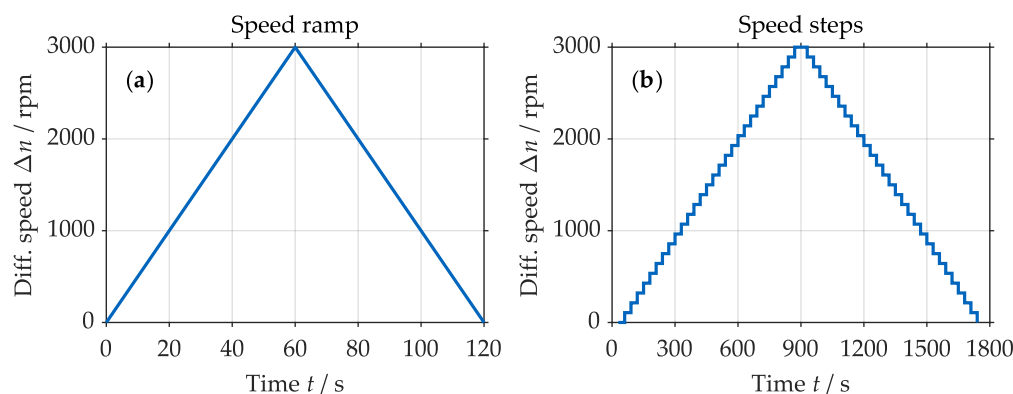


Figure 13. Different test procedures: (a) speed ramp; (b) speed steps.

In contrast, increasing the differential speed step by step (i.e., speed steps), as shown in Figure 13b, enables measuring the drag torque during constant differential speed and, thus, during steady conditions. The size and duration of the speed steps mainly define the testing time and may be adapted during testing [23]. This test procedure requires a comparatively long testing time. In Ref. [89], the testing time was reported as 45 min per single test run. In the case of the stepwise test procedure, the average drag torque during the constant differential speed steps is usually evaluated [23]. Also, a coast-down can be performed; see Ref. [42]. Here, a maximum differential speed is set, and the resulting speed-time trace is measured to determine deceleration at any given speed, which can then be used to calculate the torque loss at that speed. This procedure has been rarely applied; see Figure 11b. Several studies [38,39,68] focused on specific differential speeds and did not determine the whole drag torque curve.

During the development process, prototype test parts are necessary for experimental testing or validation of calculation models. For this purpose, plates were manufactured by 3D printing for some experimental studies [14,93,94]. A research team considered different additive manufacturing technologies (i.e., Fused Deposition Modeling (FDM), Stereolithography (SLA), Selective Laser Sintering (SLS), and PolyJet Modeling (PJM)) and materials and identified the SLA technology with epoxy resin as most suitable [94].

However, using plastic materials for manufacturing the plates may limit the maximum oil temperature to be investigated [15]. In contrast, aluminum test plates can be used for higher oil temperatures. It was found that plastic and aluminum show similar measurement results [80].

4.3.2. Characterization of Drag Loss Behavior and Systematic Investigation

Instead of the drag torque, the mean shear stress introduced in Ref. [9] is also widely used since it allows comparison of clutch systems with different plate sizes and numbers of friction interfaces or gaps [9,10,19,20,59,83,88]. Furthermore, drag losses are rarely described via power losses [9,68,71]. Characteristic points of the drag torque curve are often used to quantify the drag loss behavior, see Figure 14. The location and magnitude of the maximum and transition point of the drag loss curve are widely evaluated [1,10,19,20,23,77]. The gross torque can be used as an integral characteristic value [42]. In addition, the slope of the initial increase is used [77]. In addition, the maximum power and energy loss are rarely used as characteristic values to quantify drag loss behavior [9].

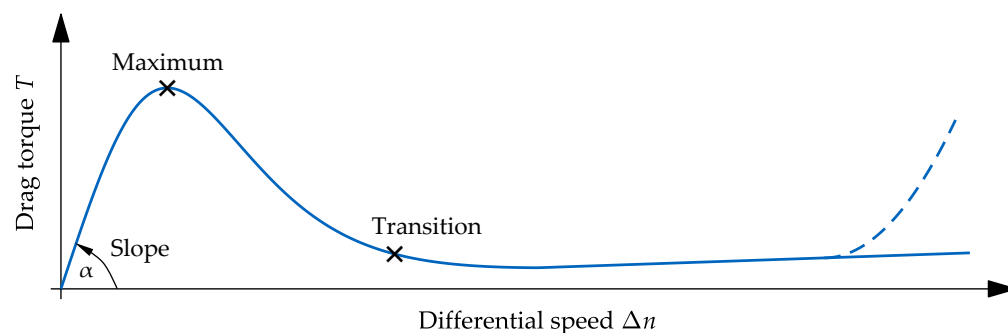


Figure 14. Characteristic drag loss values inspired by Ref. [10]. Figure adapted with permission by CC BY 4.0 (Nature). Note: Dashed line indicates potential re-increase.

Most studies varied parameters with respect to a reference parameter set to analyze their impact on drag loss behavior. Also, statistical test designs, such as full factorial [19,20,39,42,70] or mixed-level full factorial designs [10], were applied to capture the whole variety of effects and determine the main and interaction effects and statistical significance of each parameter's effect via analysis of variance (ANOVA) [19,20,39,42]. Furthermore, the Taguchi test design was applied for comprehensive analysis [87]. A multi-objective optimization algorithm was applied, e.g., to optimize the groove geometry concerning low drag torque and oil temperature rise [87].

4.3.3. Measurement of Plate Movements and Pressure Distribution

The movements of the plates, and, thus, changing clearances, influence the drag loss behavior; see Section 4.2.7. Researchers have applied distance sensors [37,41] and used digital image processing systems [95,96] to capture the plate movements. Generally, determining the 3D plate movements requires three sensors or camera systems, respectively. The sensor-based measurement of the outer plates' axial movements was realized via distance sensors mounted on the outer carrier [41]. Modifications of the plates were required, i.e., measuring points had to be integrated [41]. Another research team applied hall sensors to measure the axial and radial plate displacements [37]. Also, strain gauges were applied on the plates to differentiate between elastic deformation—which may occur at high rotational speeds—and rigid plate movements [37]. For the investigation of plate tumbling, three eddy current displacement sensors were installed on the frontmost and stationary separator plate [24]. This way, the axial displacement, and, thus, the wobbling amplitude of the frontmost friction plate, could be measured. A fast Fourier transform converts the axial displacements from time to frequency domain, enabling the identification of dominant frequencies or rotational speeds, respectively [24].

Also, the plate movements can be determined based on the image series of the clutch plates recorded during operation in the radial view. Camera systems were used to capture images of the operating clutch pack in radial view. Image processing algorithms are then applied to identify the plates and detect their edges. A high-speed camera allows the capturing of high dynamic phenomena. Displacement of the oil, and, thus, permanent optical access to the clutch plates, is realized by compressed air or a transparent displacer. However, partially oil-covered plates or air bubble formation represent significant interferences. [95,96]

Generally, determining the clearance distribution via measurement of the plate movements is challenging and costly; therefore, a statistical method [97] was developed to model the dynamically changing plate positions.

Knowing the pressure distribution occurring in the gaps during operation can be used for verifying calculation models or optimizing plate separation [80,98]. The pressure

must be measured at numerous positions to determine the two-dimensional hydrodynamic pressure distribution. Cited studies used a model-level test rig and semiconductor type or piezoresistive pressure sensors, mounted in the stationary front cover at different radii. Integrating the pressure distribution over the area gives the axial force, which can be used to optimize groove designs concerning high axial forces [80].

4.3.4. Flow Visualization and Capturing Techniques

Different flow visualization and capturing techniques have been applied to investigate the oil flow in the sub-millimeter gaps and grooves, each offering specific advantages and possibilities. When using camera-based techniques, optical access to the gap is typically required, which was realized by making the frontmost components out of transparent materials (e.g., acrylic glass). Low-distortion optical access can be reached using an anti-reflection coated float glass [11,99]. Typically, the test rig's transparent closing cover represents the frontmost plate, enabling insights into the gap. Figure 15 shows a set-up for flow visualization using a high-speed camera system.

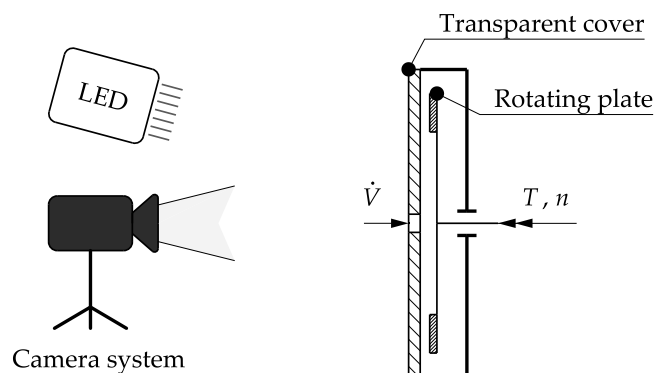


Figure 15. Schematic set-up for investigating the flow in the gap using a high-speed camera system inspired by Ref. [17]. Figure adapted with permission by CC BY 4.0 (Nature).

Table 4 provides an overview of relevant flow visualization techniques and the conditions under which they were applied.

According to Table 4, high-speed cameras were mainly used to capture the development of global flow. This relatively straightforward set-up is ideal for investigating the phenomenological flow development in the gap and grooves. However, the inability to extract velocity information underscores the need for alternative techniques.

In contrast, defocusing particle tracking velocimetry (DPTV) was found to be a reliable technique for the comprehensive analysis of complex and small flow structures of the single-phase flow. Edge and circle detection algorithms were used to determine the diameters of the recorded particle images. This measurement technique enables the gain of robust 3D3C velocity (i.e., three-dimensional, three-component) and even wall shear stress information. However, it was also mentioned that DPTV is not a standard technique as no evaluation software is commercially available. [11]

Moreover, the laser Doppler velocimetry profile sensor (LDV-PS) was successfully applied to extract 1D3C velocity (i.e., one-dimensional (circumferential), three-component) and wall shear stress information in a single-phase flow. The 1D3C velocity field was reconstructed from two consecutively measured 1D2C velocity profiles. Unlike DPTV, obtaining sufficiently precise velocity information does not require complex post-processing and evaluation. The results from LDV-PS can be further enhanced by supplementing with DPTV for a higher spatial resolution and deeper insight. [99]

Table 4. Overview of flow visualization techniques and conditions.

Ref.	Scope	Flow Visualization and Capturing Technique	Speed Range and Flow State	Groove Design and Plate Size	View Field
[38]	Flow patterns for different clearances	Camera system	1400 rpm	sb 201 mm	Close-up
[45]	Flow patterns for different rotational speeds	Camera system	{600, 1500, 2500} rpm, single- and two-phase flow	rd 153 mm	Close-up
[30]	Flow patterns for different injection flow rates	High-speed camera system	Constant speed, single- and two-phase flow	rd 153 mm	Close-up
[31,92]	Flow patterns for different rotational speeds	Camera system	{200, 500, 730, 1400, 2200} rpm, single- and two-phase flow	pl 200 mm	Close-up
[52]	Flow patterns for different variants of radial grooves	High-speed camera system	1000 rpm	pl, rd 107 mm	Close-up
[56,98]	Flow patterns for different rotational speeds and model validation	Ref. [56]: Camera system Ref. [98]: High-speed camera system	Ref. [56]: {300, 700, 1000, 1500} rpm, Ref. [98]: {150, 400, 500, 620} rpm, single- and two-phase flow	pl 197 mm	Close-up
[33]	Flow pattern and model validation	High-speed camera system	300 rpm	rd 197 mm	Close-up
[61]	Flow patterns for different rotational speeds and model validation	High-speed camera system	{200, 300, 400, 500, 700} rpm, single- and two-phase flow	rd 111 mm	Close-up
[62]	Flow patterns for different friction plate designs	High-speed camera system	{500, 1000, 1500, 4000} rpm, single- and two-phase flow	rd	Close-up
[69]	Flow patterns for different rotational speeds, injection flow rates, and clearances and model validation	High-speed camera system	{150, 180, 210} rpm, single- and two-phase flow	rd 102 mm	Close-up
[14]	Flow patterns for different rotational speeds and model validation	High-speed camera system	{500, 750, 780, 900, 1300, 1500, 2500} rpm, single- and two-phase flow	rd 155 mm	Close-up
[11,34,93]	3D3C velocity and shear stress information and model validation	Defocusing particle tracking velocimetry (DPTV) and edge and circle detection algorithms for detailed flow analysis	192 rpm, single-phase flow	rd 176 mm	Specific view fields of different magnifications
[99]	1D3C velocity and shear stress information	Laser Doppler velocimetry profile sensor (LDV-PS)	120 rpm, single-phase flow	rd 176 mm	Specific view field
[17]	Flow patterns for different oil levels	High-speed camera system	From 0 to 800 rpm, single- and two-phase flow	wf 212 mm	Entire gap and close-up

Multi-camera particle imaging techniques are unsuitable for capturing the flow due to limited optical access to the measurement domain [11]. According to Table 4, capturing the flow with high-speed cameras is the standard technique, as the set-up is comparatively simple and enables a global view of the flow in the gap and grooves. Higher-level techniques like DPTV or LDV-PS are suitable for in-depth flow analysis based on flow fields. These techniques even provide information on the local wall shear stress, which is helpful for target-oriented groove design optimization.

4.4. Methods for Calculation of Drag Losses

This review revealed that existing models for calculating the wet clutches' viscous drag losses are based on the analytical, numerical, and data-driven modeling approach. Hence, this paper grouped the models according to these modeling approaches. Additionally, few mathematical models are available for predicting drag torque due to mechanical contact at high rotational speeds [63,76,90].

4.4.1. Analytical Models

Analytical models are widely based on the Navier–Stokes equations and provide the decisive advantage of low calculation time. However, several simplifications are necessary during model development to derive the corresponding equations, bringing in decisive limitations. Widely applied simplifications and assumptions are incompressible, laminar, and steady-state flow, Newtonian fluid behavior, and axial symmetry [15,56]. Gravity and the axial flow component are typically neglected [15,56]. Analytical models are available

for only the single-phase region and the two-phase region. The majority of the models are limited to non-grooved (i.e., plain) plates. The symbols of the drag torque equations listed in the table were adapted as needed for consistency reasons. Table 5 provides an overview of relevant analytical models and their characteristics.

Table 5. Overview of relevant analytical models (sorted by year of publication in ascending order).

Ref.	Validity Range	Modeling	Drag Torque Equation	Groove Design	Validation Against
[45]	Single-phase region	Complete oil film	$T = \frac{N\mu\pi(R_0^2 - R_i^2)r_m^2\omega}{h}$	pl	Drag torque measurements
[46]	Single-phase region	Complete oil film	$T = \int_0^{2\pi} \int_{R_i}^{R_0} \frac{\nu_s}{\omega_s} r^3 AR dr d\varphi$	rd	Drag torque measurements
[12]	Single- and two-phase region	Partial oil film—equivalent radius approach, turbulent flow	$T = 2\pi \int_{R_i}^{r_0} \frac{\mu\omega r^3}{h} (1 + 0.0012Re_h^{0.94}) dr$	pl	Existing test results
[47]	Single- and two-phase region	Partial oil film—equivalent circumferential degree approach	$T = \frac{N\mu\omega}{h} \int_{R_i}^{R_0} \theta(r)r^3 dr$	pl	Existing test results
[92]	Single- and two-phase region	Partial oil film—equivalent radius approach	$T = \frac{\pi\mu\omega}{2h} (r_0^4 - R_i^4)$	pl	Drag torque measurement and high-speed camera recordings
[55]	Single- and two-phase region	Partial oil film—oil film in continuous section and oil and mist film in ruptured section	$T = \frac{N\mu\pi\omega}{2h} (r_0^4 - R_i^4) + \frac{2N\mu\pi\omega}{h} \int_{r_0}^{R_0} \phi(r)r^3 dr + \frac{2N\mu\pi\omega}{h} \int_{r_0}^{R_0} (1 - \phi(r))r^3 dr$	pl	Drag torque measurements
[54]	Single- and two-phase region	Partial oil film—equivalent radius approach	$T = \frac{N\pi\mu\omega}{2h_0} (r_0^4 - R_i^4) \delta_T$	pl	Drag torque measurement
[56]	Single- and two-phase region	Partial oil film—equivalent radius approach	$T = \frac{\alpha\mu\pi(R_0^2 - R_i^2)r_m^2\omega}{h+d_g A_g}$	rd	Drag torque measurement and camera recordings
[60,98]	Single- and two-phase region; torque re-increase [60]	Partial oil film—oil film in continuous and ruptured section	$T = \frac{\mu\pi\omega}{2h} (r_0^4 - R_i^4) + \frac{2\mu\pi\omega}{h} \int_{r_0}^{R_0} \alpha(r)r^3 dr$	pl	Drag torque measurements and high-speed camera recordings
[35,71,78]	Single- and two-phase region	Partial oil film	$T = \int_{R_i}^{r_0} \left(\frac{\mu\omega r^2}{h_p} (2\pi r - n\omega) + \frac{\mu\omega r^2}{h_g} n\omega \right) dr$	pl, gp, rd	Drag torque measurements and experimental test data
[100]	Single-phase region	Partial oil film—equivalent radius approach	$T \approx \frac{\pi\mu\omega}{2h} (r_0^4 - R_i^4)$	pl	Existing test results
[72,101]	Single- and two-phase region and torque re-increase	Partial oil film—oil film in continuous section and oil and mist film in ruptured section	$T = \frac{\mu\pi\omega}{2h_0} (r_0^4 - R_i^4) + \frac{2\mu\pi\omega}{h_0} \int_{r_0}^{R_0} \varphi r^3 dr + \frac{2\mu\pi\omega}{h_0} \int_{r_0}^{R_0} (1 - \varphi)r^3 dr$	pl, rd, sb	CFD simulation
[22]	Single- and two-phase region and torque re-increase	Partial oil film	$T = \mu\omega \sum_{i=1}^N \frac{1}{\delta_i} \int_0^{2\pi} d\beta \int_{R_i}^{r_0} \frac{r^3}{h_{ow} + r \sin \alpha \sin \beta} dr$	pl	Drag torque measurements
[82]	Single-phase region	Complete oil film	$T = \frac{\mu\pi\omega}{2h_{eq}} (R_o^4 - R_i^4)$	rd	Existing test results
[21]	Single- and two-phase region	Partial oil film—equivalent radius approach	$T = \frac{\mu\pi\omega}{2h} (r_0^4 - R_i^4) + \frac{\mu\pi\omega}{2h} (R_o^4 - r_0^4)$	pl	Drag torque measurement

Generally, a continuous oil film exists in the gaps during low differential speeds. With increasing differential speed, the oil film ruptures with rivulets' formation and is no longer continuous [12]. Figure 16a shows the complete oil film during the single-phase region, and Figure 16b shows the partial oil film after aeration during the two-phase region. The model presented in Ref. [45] is based on Newton's law of viscosity and a laminar flow and assumes a complete oil film across all speeds, making it applicable only for predicting the initial increase in the drag torque curve during the single-phase region. The authors of Ref. [46] model the drag torque reduction caused by the grooving through the percentage of the grooving area.

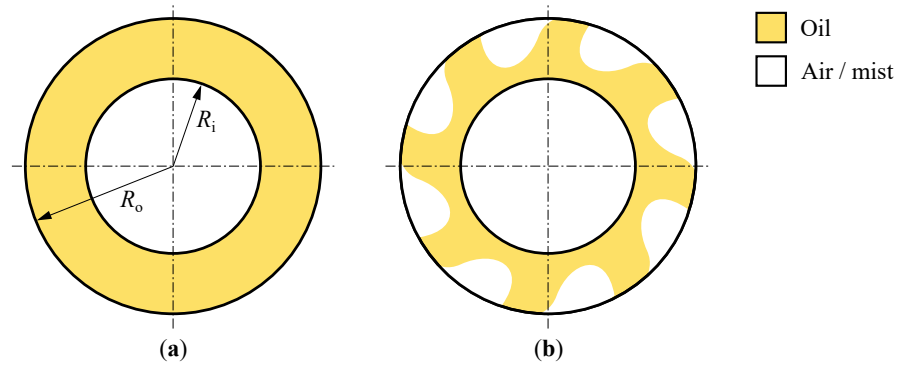


Figure 16. Different flow states: (a) single-phase flow before aeration; (b) two-phase flow after aeration. Figures adapted from Ref. [12] with permission (ASME).

Analytical models are usually based on schematics, as shown in Figure 17. It is assumed that the flow within the gap can be divided into two sections. The clearance is fully filled with oil in the section between the inner plate radius R_i and the critical radius r_0 . However, the flow is ruptured in the outer section between the critical radius and the outer plate radius R_o , resulting in a two-phase flow of air and oil. [15]

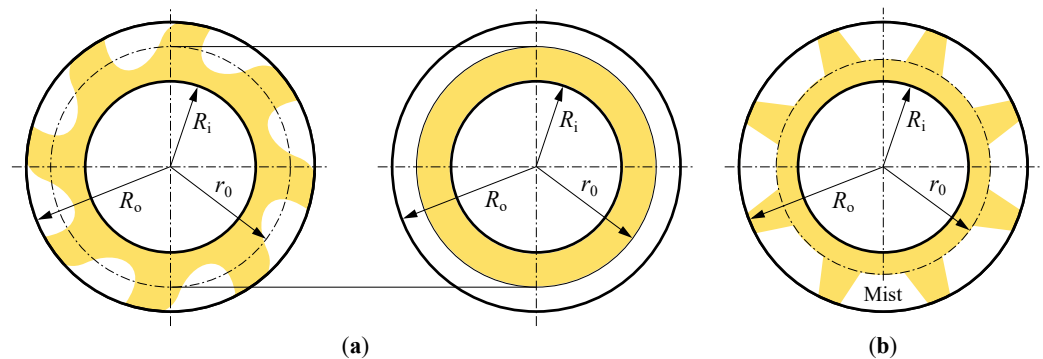


Figure 17. Modeling approaches: (a) equivalent radius approach proposed in Ref. [12]; (b) modeling approach proposed in Ref. [55]. Figures adapted with permission (ASME).

An equivalent radius approach was proposed in Ref. [12] to determine the drag torque after aeration. Here, the drag torque is determined based on a hypothetical oil film, which causes equal flow rate and drag torque of the original rivulet-shaped oil film; see Figure 17a. This approach served as groundwork for various analytical models. The respective models differ primarily in boundary conditions, assumptions regarding oil–air distribution, and the ability to take grooving into account [16].

To describe the two-phase flow, the partial oil film shape introduced by the authors of Ref. [12] was adopted, and an equivalent circumferential degree approach was proposed [47]. The model presented in Ref. [92] is also based on the equivalent radius approach. However, it uses a different approach to model the outer radius of the continuously shrinking oil film, since it was found during prior flow visualization experiments that oil only flows along the rotating plate after aeration. Hence, it is assumed that only the continuous oil film causes drag torque. In continuation of the model's development, the effects of surface tension and contact angle were considered in the model presented in Ref. [73]. The model presented in Ref. [55] also uses the radial inception of the ruptured section but also considers the drag torque contribution of the oil and mist in the ruptured section. Hence, the model combines the partial drag torques caused by the shearing of the oil in the continuous and ruptured section and the mist in the ruptured section, see Figure 17b. The model developed by the authors of Ref. [54] is based on the equivalent radius approach and incorporates a non-uniform clearance distribution through a non-uniform coefficient.

The model proposed in Ref. [56] allows for the consideration of a radial groove design through an effective clearance determined via the groove depth and percentage of groove area. This modeling approach is similar to that proposed in Ref. [82]. The models presented in Refs. [55,60,72,84,98,101] are broadly similar, with the main difference being that only the models presented in Refs. [55,72,84,101] include the drag torque contribution from the oil mist, and the models proposed in Refs. [72,101] consider a variable film thickness or clearance, which is respectively, relevant for modeling torque re-increase at high rotational speeds. The model described in Ref. [71] considers the influence of grooving via its area and shear heating. Subsequent model updates concentrated on the co- and counter-directional plate rotations [78]. In Ref. [102], scale analyses were conducted to obtain an analytical solution of the governing equations (i.e., mass and momentum conservation equations). Subsequently, dimensionless measures for drag torque, aeration onset, and other characteristics were introduced, which enable quantitative comparison of experimental data. Furthermore, a modeling approach for considering grooves was introduced. The introduced approach was then extended to consider gravitational effects [103]. In contrast to the discussed models, the authors of Ref. [104] developed an empirical approximation function of the drag torque. The function's parameters were determined via vehicle measurements. It is stated that the model's low complexity and high accuracy enable its use on electronic control units (ECUs) to consider the drag torque during shifting. A further empirical approach was proposed in Ref. [9], which uses parameters to fit analytical calculations to measurements.

The review revealed that only a few models consider the re-increase in drag torque at high rotational speed. The static pressure in the gaps decreases with rotational speed and even appears to be negative beyond a certain rotational speed [60]. Consequently, the plates are drawn closer to each other; the clearances decrease, and the drag torque re-increases [60]. The model proposed in Ref. [22] includes the effects of shrinking oil film and uneven clearances, non-uniform clearance distribution, and clearance reduction at high rotational speeds.

As shown by Table 5, analytical models are limited to the parameters of plate size, number of gaps, clearance, oil viscosity, and injection flow rate. Hence, analytical models only provide limited flexibility when considering the plates' design; they typically consider the flow between non-grooved plates or plates with simple groove designs. It was even stated that care should be taken when applying the analytical approach to complex groove geometries [78].

As part of the study presented in Ref. [15], different analytical models, namely the models proposed in Refs. [55,56,60], among others, were compared with measurements obtained with a model-level drag torque test rig. Measurements and calculations were performed for non-grooved and radially grooved friction plates and different operating parameter sets. For non-grooved friction plates, the models generally show similar results. In the single-phase region, the models showed high consistency with the measurements. However, deviations were identified for the complex flow in the two-phase region. Significant differences between the models were found for radially grooved friction plates caused by the different modeling approaches of the grooving. On top of that, significant deviations between measurement and calculations were identified. It was concluded that the investigated models do not provide satisfying results for particularly grooved friction plates. [15]

4.4.2. Numerical Models

Numerical models offer numerous advantages, like direct modeling of the grooving through discretization of the flow domain and detailed investigation of not only the integral

drag torque but also flow, phase, shear stress distribution, and even heat dissipation [14]. Additionally, numerical models enable the optimization of the clutch design in the early development stage, since there is no need for real parts [77]. However, the numerical simulation of the sub-millimeter gap flow is generally challenging and requires high computational effort. Table 6 provides an overview of selected CFD (computational fluid dynamics) models and their characteristics. Supplementary information on the models is provided in Table A1 of Appendix B.

Table 6. Overview of selected CFD models.

Ref.	Objective	Modeling	Flow Domain	Simplifications or Assumptions	Groove Design and Plate Size
[13]	Simulation of flow and investigation of speed, clearance, and flow rate	Steady-state simulation VOF model with consideration of surface tension and wall adhesion	3D—single gap 90° segment	Laminar flow assumed	pl, gp 120 mm 80 mm
[30,46]	Investigation of groove number, depth, and clearance	Ref. [46]: Single-phase model and aeration not considered Ref. [30]: VOF model with consideration of surface tension	3D—single gap 9° segment	n/a	rd 153 mm
[48]	Demonstration of aeration process based on two-phase flow model	Steady-state simulation VOF model with consideration of surface tension and wall adhesion	2D—single gap	Laminar flow assumed	pl 200 mm
[51]	Development of CFD model for calculation of flow conditions and drag torques	Cavitation model	3D—single and multiple gaps segment	n/a	rd, wf
[49]	Investigation of surface tension and contact angle	VOF model with consideration of surface tension	2D—single gap	n/a	pl 153 mm
[52]	Investigation of effect of flow field on drag torque	Single-phase model with aeration not considered	3D—single gap segment	n/a	rd 107 mm
[50]	Development of CFD modeling procedure for calculation of drag losses	Steady-state simulation VOF model with consideration of surface tension and wall adhesion	3D—single gap 22.5°/15° segments	Gravitational effects neglected, laminar flow assumed, viscous dissipation, temperature-dependent oil properties, and wall convective heat transfer considered	rd 185 mm 153 mm
[53]	Prediction of drag torque and drag decay time	Transient simulation VOF model	3D	Temperature-dependent oil properties considered	n/a
[58]	Study of two-phase flow	VOF model with consideration of surface tension and wall adhesion, turbulence modeling using RNG $k-\epsilon$ model	3D—single gap	Turbulent flow assumed, since Reynolds number $> 2.0e4$, isothermal modeling	rd 107 mm
[32]	Prediction of drag torque characteristics of two different groove designs	Steady-state simulation VOF model	3D—single gap segment	Gravitational effects neglected, laminar flow assumed	pl, rd, gp 197 mm
[57]	Investigation of various groove parameters	VOF model without consideration of surface tension, Finite Element method	3D—single gap 15° segment	Heat transfer neglected, laminar flow assumed	rd
[33]	Extended flow domain for considering oil inflow and outflow behavior	Steady-state simulation VOF model without consideration of surface tension	3D—single gap incl. carriers 90° segment	Gravitational effects neglected, laminar flow assumed, temperature dependency of oil properties considered	rd, gp 197 mm
[25]	Prediction of torque jump-up at high rotational speeds	VOF model without consideration of surface tension	3D—single gap 90° segment	Gravitational effects neglected, laminar flow assumed	pl, rd 197 mm
[61]	Investigation of drag loss behavior under consideration of detailed design features	Steady-state and transient simulation VOF model	3D—single gap incl. carriers 360° modeling	Laminar flow assumed	pl, rd 197 mm
[66]	Investigation of groove designs	Turbulence modeling using $k-\epsilon$ model	3D—single gap 15° segment	Wall surfaces of fluid and solid adiabatic	rd, sb, sp 210 mm
[14,80]	Highly detailed simulation of the flow and pressure distribution	Transient simulation VOF model with consideration of surface tension	3D—single gap 6°/90° segments	Heat conduction from fluid into solid and heat discharge into air considered, gravitational effects neglected, laminar flow assumed	pl, rd, gp-ms-wf

Table 6. Cont.

Ref.	Objective	Modeling	Flow Domain	Simplifications or Assumptions	Groove Design and Plate Size
[67]	Development of time-efficient simulation model	Steady-state simulation Coupling of single-phase and cavitation model	3D—single gap incl. inner carrier 360° modeling	Thermal and transient effects not considered	wf and gp 176 mm
[69]	Investigation of phase distributions and heat dissipation capability	Steady-state simulation VOF model with consideration of surface tension	3D—single gap 36° segment	Heat conduction of plates and heat convection between fluid and plates considered, viscous oil heating and transient effects not considered	rd 102 mm
[105]	Reliable prediction of aeration onset and drag torque as a function of rotational speed	Steady-state simulation VOF model with consideration of surface tension, rotational-speed-dependency of contact angle	2D—single gap	Gravitational effects and viscous dissipation neglected, laminar flow assumed	pl 120 mm
[77]	Comparison of cavitation and VOF model with respect to computational effort	Steady-state and transient simulation Coupling of single-phase and VOF model with consideration of surface tension or cavitation model resp.	3D—single gap incl. carriers 360° modeling	Thermal and transient effects partly considered, laminar flow assumed	wf and gp 176 mm
[79]	Investigation of non-uniform clearance distribution	Transient simulation VOF model with consideration of surface tension, turbulence modeling using RNG $k-\epsilon$ model	2D—single and multiple gaps	Temperature dependency of oil properties considered	pl 121 mm
[36]	Influence of groove structure on flow field and drag torque	n/a	3D—single gap 24° segment	n/a	rd and modified rd 97 mm
[83]	Validation of data-driven drag loss models and effects of relevant design and operating parameters	Transient simulation Coupling of single-phase and cavitation model	3D—single gap incl. carriers 360° modeling	Thermal effects not considered, laminar flow assumed	wf and gp 132 mm, 176 mm, 220 mm
[84]	Simulation of oil film shrinkage	VOF model	3D—single gap 24° segment	n/a	rd 194 mm
[87]	Thermal-fluid-solid coupling simulation for optimization of groove geometry	Steady-state simulation SST $k-\omega$ turbulence model	3D—single gap 360° modeling	n/a	rd-annular 214 mm
[106]	Fluid-structure coupled model of the entire clutch system and analysis of pressure distribution characteristics	Modeling of fluid-structure interaction	3D—multiple gaps incl. carriers 360° modeling	n/a	213 mm
[34]	Investigation of flow topology of different groove designs	Single-phase model, aeration not considered	3D—single gap 11.25° segment	Coriolis effect considered	rd and modified rd 176 mm
[86]	Investigation of groove width and depth and microgrooves	VOF model, Finite Element method	3D—single gap 360° modeling	n/a	wf 217 mm
[21]	Investigation of different operating conditions	VOF model with consideration of surface tension	3D—single gap segment	Wall surfaces adiabatic	155 mm

The review shows that the ANSYS Fluent, Star CCM+, Simerics MP+, ANSYS CFX, and OpenFOAM software were widely used for model development and simulation. To date, mesh-based methods have been primarily applied to solve the Navier–Stokes equations. In contrast, models were rarely developed based on the Reynolds equation and the Finite Difference method [44,68,74,75]. The advantage of those models is the comparatively low computational costs [68]. However, neglecting the axial flow component has a negative effect on the quality of the results [16]. The Finite Volume method is commonly used for discretizing the flow domain. However, the Finite Element method has also been applied [57,86]. The particle-based SPH (smoothed particle hydrodynamics) method has been applied only once for drag loss investigations [35]. The 3D modeling approach was mostly chosen and represents the state of the art. Two-dimensional models enable faster estimates but usually give acceptable results only for non-grooved plates [77].

As numerical simulations require high computational effort, circumferential symmetry and periodicity are often used to reduce calculation times [77]. However, the 360° modeling enables the consideration of any groove design and the replacement of only the CAD data of the groove during systematic investigations [77]. The flow domain is typically a single gap with constant clearance, axially bounded by the separator and friction plate. Some

models also include the geometry of the inner and outer carriers (i.e., cutouts for oil flow). Figure 18 depicts a typical flow domain of a CFD model and its boundary conditions.

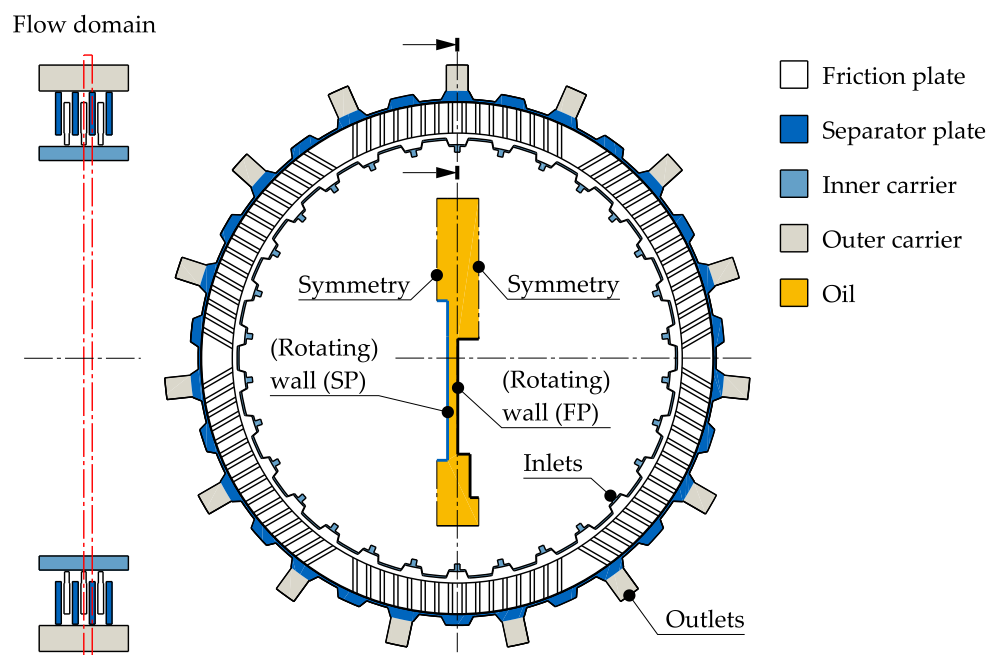


Figure 18. Representative 360° flow domain and boundary conditions of CFD model presented in Ref. [77]. Figure adapted with permission (SAE). Note: Flow domain and boundary conditions typically differ between existing CFD models.

In contrast, a fluid–structure coupled model not only determines the drag losses of the whole wet clutch system but also enables the analysis of the plates’ motion process and exploration of dynamic characteristics [106]. The VOF (volume of fluid) model, proposed in Ref. [107], is commonly applied for modeling the complex two-phase flow. The models based on this show a good correlation between simulation and measurement [67]. However, the VOF model requires high computing costs, so the geometry is often simplified [77]. In contrast, the cavitation (based on Ref. [108]) and mixture models are rarely applied. Those models consider the viscosity of the oil–air mixture and provide lower computational effort [67]. It was found that the cavitation approach is more suitable for most engineering applications due to its balanced trade-off between computational demand and accuracy [77].

It was found that gravitational effects can be neglected during modeling since centrifugal acceleration on the fluid resulting from high speeds dominates [14]. Modeling heat conduction from the oil into the solid bodies and heat discharge into the air is highly significant for considering shear heating and simulations of high temperatures [14]. Critical Reynolds numbers of 1400 [33] and 2000 [55] are used. The models widely assume a laminar flow, as the Reynolds numbers are low in the speed range of interest [13,14]. This review revealed that oil is usually modeled as incompressible. In contrast, air is modeled as compressible or incompressible, depending on the modeling approach. However, incompressible formulation of the air flow may lead to non-physical solutions [105]. For considering plate movements caused by, for instance, changes in the pressure field, mesh morphing can be applied [25]. This way, the re-increase in drag torque at high rotational speeds can be investigated. A statistical method for determining the clearance distribution was coupled with a CFD model for a simulation-based investigation of the effect of non-uniform clearance distribution in the two-phase region [79].

The simulation models are typically validated against drag torque measurements and high-speed flow recordings conducted as part of the study or against existing experimental data.

During validation, particular emphasis needs to be placed on minimizing deviations of the input parameters of the drag torque measurements as the simulation model relies on exact inputs. These include, among other things, determining the exact groove geometries while including production-related variations, ensuring a uniform axial clearance distribution, reducing fluctuations in oil temperature and injection flow rate, and verifying the oil characteristics. [67]

Model-level test rigs were primarily used for validation. Those test rigs enable the precise setting of the operating parameters and oil supply, leading to a high reproducibility of the flow behavior and enabling easy optical access to the gap by using a transparent front cover [14]. Depending on the design of the inner carrier, it may not be guaranteed that the oil is only supplied to the gaps when using a component-level test rig [77]. When using a component-level test rig, the measured drag torque of the entire clutch system is typically divided by the number of gaps for validation.

The computational resources necessary for CFD simulation are commonly high, but calculation times are rarely reported in relevant papers. Using the less calculation-intensive cavitation model for calculating the drag torque curve results in calculation times of 14 h to 20 h on a workstation with eight cores [67]. The calculation-intensive VOF model causes approx. five-times-higher calculation times [77]. However, computational effort was rated even as extremely high when considering various effects and complex geometries [14].

4.4.3. Data-Driven Models

Following current trends, machine learning algorithms were also used to build powerful drag loss models based on experimental or simulation data. Generally, data-driven models enable fast and accurate drag loss predictions. Therefore, these models can be used, for example, for clutch development or as part of a full drivetrain simulation model. However, data generation can be time-consuming. A significant advantage of the data-driven approach is that there are no limitations regarding the complexity of the physical effects to be modeled. [89]

For building a data-driven drag loss model, the universally applicable methodology proposed in Ref. [23] can be applied. The methodology covers all necessary steps from data generation to model application. Data generation for subsequent data-driven modeling was also focused on by Ref. [10]. Table 7 provides an overview of data-driven models and their characteristics.

The drag loss model presented in Ref. [106] is based on CFD simulation data and was trained using a direct artificial neural network (DANN). The model enables direct predictions of the drag torque. The model's structure is depicted in Figure 19a. In contrast, the drag loss models presented in Refs. [83,88,89] are based on experimental data and predict four characteristic drag loss values, which are subsequently used as support points to approximate the drag torque curve. The drag loss models were built according to the methodology proposed in Ref. [23]. Generation of the dataset required approx. 200 h of net testing time [89]. The models' structure is depicted in Figure 19b. Support vector regression, symbolic regression, and Gaussian process regression (GPR) were considered for model building [89]. However, it was finally found that GPR best meets the requirements of flexibility and interpretability. The drag loss models were validated from an engineering perspective against existing knowledge.

Table 7. Overview of data-driven models (sorted by year of publication in ascending order). Note: IL, injection lubrication; DL, dip lubrication; BM, brake operation mode, CM, clutch operation mode.

Ref.	Scope of Application	Input and Output	Algorithm	Dataset	Performance
[59]	Probability of plate tumbling	Input: 3 operating parameters Output: Probability of plate tumbling	Artificial neural network (ANN)	n/a	n/a
[83]	Drag loss curve under IL and BM	Input: 7/9 operating and design parameters Output: 4 char. drag loss values and approximated drag loss curve	Gaussian process regression (GPR)	Experiment; 492 measurements	SD = 14.9–28.2%
	Drag loss curve under IL and CM			Experiment; 133 measurements	SD = 27.4–47.9%
	Drag loss curve under DL and BM			Experiment; 254 measurements	SD = 6.8–25%
[106]	Drag torque under IL	Input: 5 operating parameters Output: Drag torque	Direct artificial neural network (DANN)	Simulation; 5042 data samples	MSE = 4.6 (Nm) ²
[88]	Drag loss curve under IL and BM	Input: 7/9 operating and design parameters Output: 4 char. drag loss values and approximated drag loss curve	Gaussian process regression (GPR)	Experiment; 561 measurements	SD = 16.6–24.9%
	Drag loss curve under IL and CM			Experiment; 446 measurements	SD = 17.2–41.2%
	Drag loss curve under DL and BM			Experiment; 401 measurements	SD = 5.6–18.8%
[89]	Drag loss curve under DL and BM	Input: 7 operating and design parameters Output: 4 char. drag loss values and approximated drag loss curve	Gaussian process regression (GPR)	Experiment; 276 measurements	R ² = 0.84–0.95 MRE = 4.6–14.2%

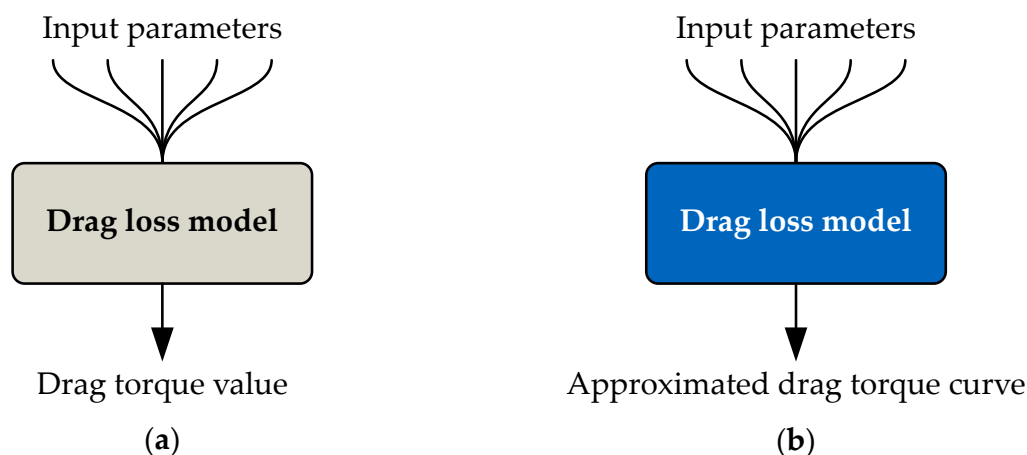


Figure 19. Structures of existing data-driven drag loss models: (a) drag loss model proposed in Ref. [106]; (b) drag loss model proposed in Ref. [89]. Sub-figure (a) adapted with permission (Springer) and Sub-figure (b) with permission by CC BY 4.0 (Elsevier).

5. Discussion

The review shows that fundamental knowledge of wet clutches’ drag loss behavior is available. However, the authors found that further research is still required to improve the overall understanding and reduce drag losses. The research needs (RNs) drawn up are listed below. The Shifting Elements and Electro-mechanical Drives research group of the Gear Research Center (FZG) of the Technical University of Munich intends to focus their further research on the identified research gaps to advance the current state of research.

RN-1	Simulation-based analysis of oil flow during dip lubrication
	<p>The review revealed that the vast majority of research was conducted based on injection lubrication; see Figure 8c. In contrast, only a few studies have focused on dip lubrication, although this lubrication type is also widely used. Recently published studies [10,17] analyzed the flow and drag torque generation and investigated the integral drag loss behavior influenced by various geometry and operating parameters using experimental methods. The authors of this paper see high potential in applying CFD simulation to extend knowledge of the flow phenomena in sub-millimeter gaps and grooves and the effects of relevant design and operating parameters. However, developing a time-efficient CFD model is considered challenging, mainly due to the local immersion of the plates. This means that no periodicities can be applied to reduce model size. It is assumed that transient flow modeling is required. The VOF approach may be the tool of choice.</p>
RN-2	Data-driven prediction of torque jump-up
	<p>Most studies focused on the hydrodynamic drag losses occurring in the low- and mid-rotational speed regions. In contrast, comparably few studies were conducted on the sudden re-increase in drag torque in the high rotational speed region, see Table 3. Following the current trends towards increasing rotational speeds of particularly automotive drivetrains, the abrupt increase in drag loss may be the focus of future research. It was reported that the torque jump-up is not always repeatable [59] and may be based on chance, making computational investigation more difficult. Hence, future research could focus on the data-driven prediction of the torque jump-up. To date, a data-driven model for predicting the probability of plate tumbling has only been presented in Ref. [59]. However, the authors of this paper see potential in using modern classification algorithms to predict the occurrence of sudden drag torque increase under a comprehensive set of design and operating parameters. Regression algorithms could be used to predict the rotational speed of torque jump-up.</p>
RN-3	Image-based analysis of 3D plate movements
	<p>Various papers [24,59] report that plates perform tumbling movements under certain operating conditions. However, to the authors' knowledge, those movements and their effects on the drag losses have not been investigated on a fundamental level for entire clutch systems and real-world operating conditions. Hence, future research could focus on the 3D plate movements by applying a recently published image-based measurement set-up and methodology [96]. Upgrading the proposed test set-up to three camera systems enables researchers to fundamentally analyze the 3D plate movements and the circumferential clearance variation in real clutch systems.</p>
RN-4	Simulation-based analysis of plate separation process under external forces
	<p>In non-stationary applications, external forces resulting from vehicle dynamics or vibrations act on the plates, influencing the drag loss behavior. In the case of stationary applications, external forces originate from a non-horizontal installation position. A recently published paper [20] on the integral drag loss and plate separation behavior showed that the plates separate even under external forces. However, it was found that the drag losses are higher as the clearances between adjacent plates are generally smaller. The plate separation process, mainly driven by hydrodynamic forces, has yet to be fundamentally investigated for applications with external forces acting on the plates. The authors of this paper see high potential in applying CFD simulation to investigate the plate separation process. This requires the entire clutch system to be considered and the fluid–structure interaction to be modeled.</p>

RN-5	Investigation of carrier design and spline contact on drag loss behavior
	The review showed that prior research has not considered the influence of the carrier design (i.e., oil inlet and outlet geometry and sectional area or backlash and pitch error of spline contact, etc.) sufficiently, see Table 3. Screening tests showed that the sectional area of the oil inlets and outlets represents a significant design parameter for reducing drag losses [59]. It is assumed that a small sectional area of the oil outlet holes hinders the oil from draining out of the clutch system [59]. Furthermore, the authors of this paper assume that an inadequate radial and circumferential backlash or pitch error of the spline hinders the plates from moving freely, which may result in non-uniform clearance distribution and reduced clearance utilization rate. Overall, the authors see high potential in optimizing the carrier design and spline contact for significant drag loss reduction.
RN-6	Investigation of plate size on drag loss behavior
	The review revealed that research was mainly conducted on plate sizes (i.e., mean plate diameter) ranging from 100 mm to 250 mm, see Figure 10a. However, plates of a higher mean diameter are also widely applied across various sectors. To date, it has not been clarified whether the existing knowledge can be transferred to larger clutch systems. Hence, the authors of this paper recommend investigating large diameter sizes and masses. However, as experimental testing is more difficult with increasing plate sizes, CFD simulation may be the tool of choice to conduct investigations without limitations.
RN-7	Investigation of sub-zero temperatures on drag loss behavior
	Existing research results are limited primarily to oil temperatures in the positive range, see Figure 10c. However, sub-zero oil temperatures can also occur in various applications and operating phases. High drag torques are expected in this temperature range due to the high oil viscosity. This reduces the drivetrain's efficiency but can also for example, lead to malfunction or safety restrictions due to the unintentional drag of decoupled drivetrains. Today, there is little knowledge of the drag loss behavior under sub-zero oil temperatures, which is why the authors of this paper recommend conducting further research.
RN-8	Scoping review of in-depth flow characteristics
	The present review focused on methods for determining wet clutches' drag losses and the integral effects of design and operating parameters on drag loss behavior. However, experimental and simulation-based studies also provide significant knowledge of the flow characteristics in the sub-millimeter gaps and grooves. Hence, summarizing the current body of literature focusing on flow characteristics would complement the present scoping review and aid researchers and engineers in developing efficient wet clutch systems.

Limitations

In this scoping review, only documents available in databases were considered, while non-indexed literature, such as unpublished reports, institutional documents, or independently hosted materials, was not included. Hence, the paper might not fully reflect the full range of existing knowledge. Further, it needs to be mentioned that data extraction was conducted to the best of the authors' abilities and followed a predefined framework to minimize errors. However, the possibility of unintentional errors cannot be completely ruled out. Any inaccuracies identified post-publication will be addressed appropriately.

6. Conclusions

The present paper constitutes the first scoping review on wet brakes' and clutches' drag loss behavior and provides a detailed summary of the current state of research on this

topic. The review process involved a systematic and manual database search, leading to a set of 93 documents for final analysis. The review shows that wet brakes' and clutches' drag losses have been the subject of research since the 1970s, with a growing interest in this field of research in the last 15 years. Drag loss research has been mainly driven by the automotive sector. This is assumed to be the main reason most studies were conducted for injection lubrication. Generally, experimental studies were performed to investigate the integral drag losses and flow characteristics and validate calculation models. Calculations are based on numerical, analytical, and data-driven modeling approaches, with the data-driven approach being established in recent years and promising fast and accurate drag loss prediction. The review revealed a comprehensive knowledge of parameter effects on the drag loss behavior. Several research needs were identified and are provided.

Author Contributions: Conceptualization, L.P.-G.; methodology, L.P.-G.; formal analysis, L.P.-G.; writing—original draft preparation, L.P.-G.; writing—review and editing, K.V. and K.S.; visualization, L.P.-G.; supervision, K.V. and K.S. All authors have read and agreed to the published version of the manuscript.

Funding: This research received no external funding.

Data Availability Statement: Data sharing is not applicable.

Conflicts of Interest: The authors declare no conflicts of interest.

Abbreviations

AE	Air entrainment
ANN	Artificial neural network
ANOVA	Analysis of variance
BM	Brake operation mode
CA	Calculation-based
CD	Carrier design
CFD	Computational fluid dynamics
CM	Clutch operation mode
CPU	Central processing unit
DANN	Direct artificial neural network
DL	Dip lubrication
DPTV	Defocusing particle tracking velocimetry
ECU	Electronic control unit
EX	Experimental
FVA	Research Association for Drive Technology e. V.
FZG	Gear Research Center
gp	Group-parallel groove design
GPR	Gaussian process regression
IL	Injection lubrication
LDV-PS	Laser Doppler velocimetry profile sensor
NVH	Noise, vibration, harshness
OT	Oil type
pl	Plain or non-grooved
PRISMA	Preferred reporting items for systematic reviews and meta-analyses
rd	Radial groove design

RN	Research need
sb	Sunburst groove design
sp	Spiral groove design
SPH	Smoothed particle hydrodynamics
wf	Waffle groove design
VOF	Volume of fluid

Nomenclature

Symbol	Unit	Meaning
A	m^2	Area
A_g	–	Groove area percentage
AR	–	Area ratio of grooved plate
d_g	m	Groove depth
h	m	Clearance
h_{eq}	m	Equivalent clearance
h_g	m	Distance top of the friction pads and separator plate
h_{ow}	m	Clearance under axial contraction
h_p	m	Distance groove base and separator plate
h_0	m	Average clearance, real film thickness
MRE	–	Mean relative error
MSE	$(Nm)^2$	Mean squared error
n	rpm, –, –	Rotational speed, number of grooves, number of records
N	–	Number of gaps
p_i	Pa	Pressure at inner diameter
p_o	Pa	Pressure at outer diameter
r	m	Radial coordinate
r_m	m	Mean plate radius
r_0	m	Critical radius
R_i	m	Inner plate radius
R_o	m	Outer plate radius
R^2	–	Coefficient of determination
Re	–	Reynolds number
SD	–	Standard deviation
t	s	Time
T	Nm	Drag torque
\dot{V}	m^3/s	Injection flow rate
v_s	m/s	Tangential component of velocity scale
w	m	Groove width
w_s	m/s	Axial component of velocity scale
α	–, °, Nm/rpm	Oil volume fraction, inclination angle, slope
β	°	Angular/tangential coordinate
$\dot{\gamma}$	1/s	Shear rate
δ_T, δ_i	–	Non-uniform coefficient
Δn	rpm	Differential speed
θ	°	Oil film circle area
μ	Pa·s	Dynamic oil viscosity
μ_M	Pa·s	Dynamic mist viscosity
τ	MPa	Shear stress
φ	°	Angular/tangential coordinate
ϕ	–	Wetted fraction of oil film
ω	1/s	Angular velocity

Appendix A

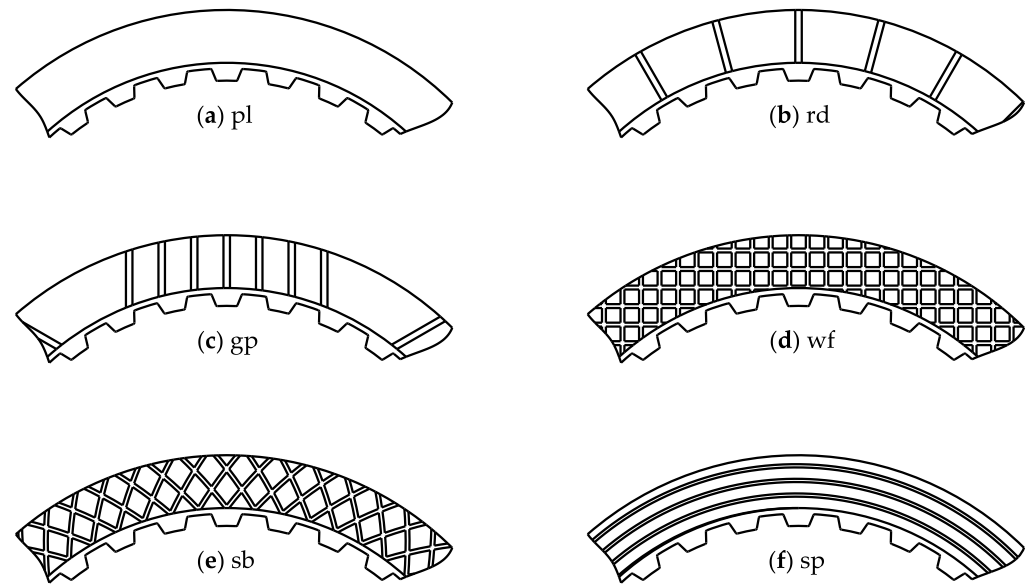


Figure A1. Groove designs: (a) plain or non-grooved; (b) radial; (c) group-parallel; (d) waffle; (e) sunburst; (f) spiral.

Appendix B

Table A1. Supplementary information on selected CFD models.

Ref.	Boundary Conditions	Lubrication Type	Validation Against	Mesh Size	Computational Effort	Software
[13]	Inlet: Velocity BC Outlet: Pressure BC Plates: (Moving) wall BC Other: Periodic BC	Injection lubrication	Drag torque measurement	Between 4800 and 52,000 cells (hexahedral)	n/a	Fluent 6.0
[30,46]	Inlet: Natural BC Outlet: Pressure BC Plates: No-slip BC Other: Periodic BC	Injection lubrication	Drag torque measurements	n/a	n/a	Fluent
[48]	Inlet: Mass flow BC Outlet: Pressure BC Plates: (Rotating) wall BC	Injection lubrication	Drag torque measurement	9000 quadrilateral cells	n/a	Fluent
[51]	Inlet and outlet: Flow rate and pressure BC	Injection lubrication	High-speed recordings	n/a	n/a	ANSYS CFX
[49]	Inlet: Natural BC Outlet: Pressure BC	Injection lubrication	Drag torque measurements	n/a	n/a	Fluent
[52]	Inlet: Velocity and Neumann pressure BC Outlet: Pressure BC	Injection lubrication	Drag torque measurements	n/a	n/a	OpenFOAM
[50]	Inlet: Velocity BC Outlet: Pressure BC Plates: (Moving) wall BC Other: Periodic BC	Injection lubrication	Existing test results	50,000 cells (hexahedral)	n/a	Fluent 12.r.1

Table A1. Cont.

Ref.	Boundary Conditions	Lubrication Type	Validation Against	Mesh Size	Computational Effort	Software
[53]	Inlet: Initially flow rate BC, after closing of oil supply wall BC Plates: (Moving) wall BC	Injection lubrication	Drag torque measurement	n/a	n/a	STAR-CCM+
[58]	Inlet: Mass flow BC Outlet: Pressure BC	Injection lubrication	Existing test results	472,752 elements	n/a	Fluent 6.1
[32]	Inlet: Velocity BC (oil volume fraction 1) Outlet: Pressure BC (oil volume fraction 0) Other: Periodic BC	Injection lubrication	Drag torque measurements	Hexahedral mesh	n/a	STAR-CCM+
[57]	Inlet: Flow BC Other: Periodic BC	Injection lubrication	n/a	n/a	n/a	n/a
[33]	Inlet: Velocity BC (oil volume fraction 1) Outlet: Pressure BC (oil volume fraction 0) Plates: (Moving) wall BC Other: Periodic BC	Injection lubrication	Drag torque measurements and high-speed recordings	Hexahedral mesh	Reported that results available within several hours	STAR-CCM+
[25]	Inlet: Velocity BC (oil volume fraction 1) Outlet: Pressure BC (oil volume fraction 0) Plates: Rotating reference frame Other: Periodic BC	Injection lubrication	Drag torque measurements	n/a	Calculation time significantly increases when using mesh morphing	STAR-CCM+
[61]	Inlet: Mass flow BC (oil volume fraction 1) Outlet: Neumann BC for pressure and phase fraction	Injection lubrication	Drag torque measurements and high-speed recordings	More than 4 million hexahedral cells	n/a	n/a
[66]	Other: Periodic BC	Injection lubrication	Drag torque measurements	Between 75,000 and 80,000 cells (hex dominant)	n/a	CFX
[14,80]	Inlet: Velocity BC; mass flow and pressure BC Outlet: Pressure BC Solid surfaces: No-slip BC Other: Periodic BC and temperature BC for outer plate surface and reverse flow	Injection lubrication	Drag torque measurements, high-speed recordings, and pressure measurements	Between 80,000 and 1.6 million cells (regular hexahedral)	High calculation times reported	ANSYS Fluent 17.2
[67]	Inlet: Pressure BC or volume flow BC resp. Outlet: Pressure BC Plates: Rotating wall BC Other: Symmetry BC in axial direction	Injection lubrication	Drag torque measurements	1.7 million cells (created with binary tree mesh technique)	Drag torque curve on workstation with eight CPU cores in 14 h to 20 h	Simerics MP+
[69]	Inlet: Mass flow BC Outlet: Pressure BC Plates: (Rotating) wall BC Other: Periodic BC	Injection lubrication	Camera recordings	307,644 cells	n/a	ANSYS Fluent 15.0

Table A1. Cont.

Ref.	Boundary Conditions	Lubrication Type	Validation Against	Mesh Size	Computational Effort	Software
[105]	Inlet: Mass flow BC Outlet: Pressure BC Plates: No-slip BC and no and heat flux Other: Temperature and pressure BC for reverse flow	Injection lubrication	Drag torque measurement	106,400 nodes	n/a	ANSYS Fluent 17.2
[77]	Inlet: Pressure BC or mass flow BC resp. Outlet: Pressure BC Plates: Rotating wall BC Other: Symmetry BC in axial direction	Injection lubrication	Drag torque measurements	3.5 million cells (created with binary tree mesh technique)	Whole drag torque curve on workstation: 12 h for cavitation model and 64 h for VOF model	Simerics MP+
[79]	Inlet: Volume flow BC Outlet: Pressure BC	Injection lubrication	n/a	n/a	n/a	ANSYS Fluent
[36]	Inlet: Velocity BC Outlet: Pressure BC Other: Periodic BC	Injection lubrication	n/a	n/a	n/a	n/a
[83]	Inlet: Pressure BC or volume flow BC resp. Outlet: Pressure BC Plates: Rotating wall BC Other: Symmetry BC in axial direction	Injection lubrication	Drag torque measurements	n/a	n/a	Simerics MP+
[84]	Inlet: Velocity BC Outlet: Pressure BC Plates: Active and passive wall BC Other: Periodic BC	Injection lubrication	Drag torque measurements and calculations	n/a	n/a	n/a
[87]	Inlet: Mass flow BC Outlet: Outflow BC Plates: (Rotating) wall BC	Injection lubrication	Existing test results	n/a	n/a	Fluent
[106]	n/a	Injection lubrication	n/a	Element size fluid domain: 0.5 mm, solid domain 3 mm	Reported that calculation time is very long	ANSYS Workbench
[34]	Inlet: Velocity BC Outlet: Pressure BC Plates: (Rotating) wall BC Other: Periodic BC	Injection lubrication	DPTV measurements	Between 1 and 2.5 million cells	n/a	OpenFOAM
[86]	Inlet: Velocity BC Outlet: Pressure BC Plates: (Rotating) wall BC	Injection lubrication	n/a	n/a	n/a	n/a
[21]	Inlet: Velocity BC Outlet: Pressure BC Plates: (Rotating) wall BC	Injection lubrication	Drag torque measurements	Structured hexahedron mesh	n/a	Fluent

References

1. Iqbal, S.; Al-Bender, F.; Pluymers, B.; Desmet, W. Experimental Characterization of Drag Torque in Open Multi-Disks Wet Clutches. *SAE Int. J. Fuels Lubr.* **2013**, *6*, 894–906. [[CrossRef](#)]
2. Walker, P.D.; Zhang, N.; Tamba, R.; Fitzgerald, S. Simulations of drag torque affecting synchronisers in a dual clutch transmission. *Jpn. J. Indust. Appl. Math.* **2011**, *28*, 119–140. [[CrossRef](#)]

3. Park, K.; Kang, M.; Lee, J.; Son, W.C.; Harianto, J.; Kahraman, A. *Development of an Analysis Program to Predict Efficiency of Automotive Power Transmission and Its Applications*; SAE Technical Paper; SAE: Warrendale, PA, USA, 2018; No. 2018-01-0398. [[CrossRef](#)]
4. Zhou, X.; Walker, P.; Zhang, N.; Zhu, B.; Ruan, J. Numerical and experimental investigation of drag torque in a two-speed dual clutch transmission. *Mech. Mach. Theory* **2014**, *79*, 46–63. [[CrossRef](#)]
5. Vacca, F.; De Pinto, S.; Hartavi Karci, A.E.; Gruber, P.; Viotto, F.; Cavallino, C.; Rossi, J.; Sornioti, A. On the Energy Efficiency of Dual Clutch Transmissions and Automated Manual Transmissions. *Energies* **2017**, *10*, 1562. [[CrossRef](#)]
6. Mileti, M.; Pointner, L.; Fischer, P.D.; Pflaum, H.; Stahl, K. Dynamic analysis of powershifts with form-fit clutches in automatic transmissions. *Int. J. Powertrains* **2021**, *10*, 218–234. [[CrossRef](#)]
7. Gu, X.; Takabayashi, H.; Fujii, T.; Nishida, M.; Ishikawa, K. *Latest Technologies Applied to Automatic Transmission Maji-BandTM*; SAE Technical Paper; SAE: Warrendale, PA, USA, 2006; No. 2006-01-0356. [[CrossRef](#)]
8. Page, M.J.; McKenzie, J.E.; Bossuyt, P.M.; Boutron, I.; Hoffmann, T.C.; Mulrow, C.D.; Shamseer, L.; Tetzlaff, J.M.; Akl, E.A.; Brennan, S.E.; et al. The PRISMA 2020 statement: An updated guideline for reporting systematic reviews. *BMJ* **2021**, *372*, n71. [[CrossRef](#)]
9. Draexl, T.; Pflaum, H.; Stahl, K. *FVV No. 1012—Schleppverluste Lamellenkupplungen: Wirkungsgradverbesserung durch Reduzierung der Schleppverluste an Lamellenkupplungen*; Final Report; FVA: Frankfurt am Main, Germany, 2013.
10. Pointner-Gabriel, L.; Menzel, M.; Voelkel, K.; Schneider, T.; Stahl, K. Experimental investigation of drag loss behavior of dip-lubricated wet clutches for building a data-driven prediction model. *Sci. Rep.* **2024**, *14*, 9241. [[CrossRef](#)]
11. Leister, R.; Fuchs, T.; Mattern, P.; Kriegseis, J. Flow-structure identification in a radially grooved open wet clutch by means of defocusing particle tracking velocimetry. *Exp. Fluids* **2021**, *62*, 29. [[CrossRef](#)]
12. Yuan, Y.; Liu, E.A.; Hill, J.; Zou, Q. An Improved Hydrodynamic Model for Open Wet Transmission Clutches. *J. Fluids Eng.* **2007**, *129*, 333–337. [[CrossRef](#)]
13. Yuan, Y.; Attibele, P.; Dong, Y. *CFD Simulation of the Flows Within Disengaged Wet Clutches of an Automatic Transmission*; SAE Technical Paper; SAE: Warrendale, PA, USA, 2003; No. 2003-01-0320. [[CrossRef](#)]
14. Neupert, T.; Bartel, D. High-resolution 3D CFD multiphase simulation of the flow and the drag torque of wet clutch discs considering free surfaces. *Tribol. Int.* **2019**, *129*, 283–296. [[CrossRef](#)]
15. Neupert, T.; Benke, E.; Bartel, D. Parameter study on the influence of a radial groove design on the drag torque of wet clutch discs in comparison with analytical models. *Tribol. Int.* **2018**, *119*, 809–821. [[CrossRef](#)]
16. Neupert, T. *Strömungsuntersuchungen an geöffneten nasslaufenden Kupplungslamellen*. Ph.D. Thesis, Otto-von-Guericke-Universität Magdeburg, Magdeburg, Germany, 2021.
17. Pointner-Gabriel, L.; Schermer, E.; Schneider, T.; Stahl, K. Experimental analysis of oil flow and drag torque generation in disengaged wet clutches. *Sci. Rep.* **2023**, *13*, 17193. [[CrossRef](#)] [[PubMed](#)]
18. Oerleke, C.; Funk, W. *FVA No. 290—Leerlaufverhalten von ölgekühlten Lamellenkupplungen*; Final Report; FVA: Frankfurt am Main, Germany, 1998.
19. Pointner-Gabriel, L.; Forleo, C.; Voelkel, K.; Pflaum, H.; Stahl, K. *Investigation of the Drag Losses of Wet Clutches at Dip Lubrication*; SAE Technical Paper; SAE: Warrendale, PA, USA, 2022; No. 2022-01-0650. [[CrossRef](#)]
20. Pointner-Gabriel, L.; Flamm, S.; Menzel, M.; Voelkel, K.; Stahl, K. Experimental investigation of drag loss and plate separation behavior of wet clutches under external forces. *Results Eng.* **2024**, *24*, 102918. [[CrossRef](#)]
21. Li, J.; Ma, C.; Wang, X.; Lan, H.; Wang, Z. Study on drag torque characteristics of wet multiplate clutch under high-speed operating condition. *Proc. Inst. Mech. Eng. Part D J. Automob. Eng.* **2023**. [[CrossRef](#)]
22. Shi, L.; Ma, B.; Wu, J.; Yan, X.; Li, H. The influence of inertia resistance on the drag torque in the wet multi-disk clutch with splined connected restriction. *IOP Conf. Ser. Mater. Sci. Eng.* **2019**, *612*, 032141. [[CrossRef](#)]
23. Pointner-Gabriel, L.; Voelkel, K.; Pflaum, H.; Stahl, K. A methodology for data-driven modeling and prediction of the drag losses of wet clutches. *Forsch Ingenieurwes* **2023**, *87*, 555–570. [[CrossRef](#)]
24. Hou, S.; Hu, J.; Peng, Z. Experimental Investigation on Unstable Vibration Characteristics of Plates and Drag Torque in Open Multiplate Wet Clutch at High Circumferential Speed. *J. Fluids Eng.* **2017**, *139*, 111103. [[CrossRef](#)]
25. Mahmud, S.F.; Pahlovy, S.A.; Kubota, M.; Ogawa, M.; Takakura, N. *A Simulation Model for Predicting High Speed Torque Jump Up Phenomena of Disengaged Transmission Wet Clutch*; SAE Technical Paper; SAE: Warrendale, PA, USA, 2017; No. 2017-01-1139. [[CrossRef](#)]
26. Elsevier, B.V. Scopus. Available online: <https://www.scopus.com> (accessed on 2 December 2024).
27. Clarivate PLC. Web of Science. Available online: <https://www.webofscience.com> (accessed on 2 December 2024).
28. FVA e. V. THEMIS. Available online: <https://fva-net.de/service/themis> (accessed on 2 December 2024).
29. Ouzzani, M.; Hammady, H.; Fedorowicz, Z.; Elmagarmid, A. Rayyan—A web and mobile app for systematic reviews. *Syst. Rev.* **2016**, *5*, 210. [[CrossRef](#)]

30. Aphale, C.R.; Schultz, W.W.; Ceccio, S.L. The Influence of Grooves on the Fully Wetted and Aerated Flow Between Open Clutch Plates. *J. Tribol.* **2010**, *132*, 011104. [[CrossRef](#)]
31. Hu, J.; Peng, Z.; Wei, C. Experimental Research on Drag Torque for Single-plate Wet Clutch. *J. Tribol.* **2012**, *134*, 014502. [[CrossRef](#)]
32. Mahmud, S.F.; Pahlovy, S.A.; Kubota, M.; Ogawa, M.; Takakura, N. *Multi-Phase Simulation for Predicting Better Groove Pattern of the Clutch Disk for Low Drag Torque*; SAE Technical Paper; SAE: Warrendale, PA, USA, 2015; No. 2015-01-1977. [[CrossRef](#)]
33. Mahmud, S.F.; Pahlovy, S.A.; Kubota, M.; Ogawa, M.; Takakura, N. *Multi-Phase Simulation for Studying the Effect of Different Groove Profiles on the Drag Torque Characteristics of Transmission Wet Clutch*; SAE Technical Paper; SAE: Warrendale, PA, USA, 2016; No. 2016-01-1144. [[CrossRef](#)]
34. Sax, C.; Stroth, A.; Leister, R.; Denda, C.; Buerk, P.; Dreisbach, M.; Kriegseis, J. Fluid-mechanical evaluation of different clutch geometries based on experimental and numerical investigations. *Forsch Ingenieurwes* **2023**, *87*, 1297–1306. [[CrossRef](#)]
35. Szalai, G.; Ray, R.; Bansal, H.; Leighton, M. *Wet Clutch Drag Loss Simulation for Different Clutch Patterns*; SAE Technical Paper; SAE: Warrendale, PA, USA, 2022; No. 2022-01-1118. [[CrossRef](#)]
36. Wang, C.; Ding, W.; Zheng, X.; Zhu, H.; Tian, Z.; Xie, F.; Gao, K. Simulation and experimental study on the influence of oil groove structure on the drag torque of the wet clutch. *Ind. Lubr. Tribol.* **2021**, *73*, 846–854. [[CrossRef](#)]
37. Klausner, M.; Funk, W. *FVA No. 117—Lamellentaumeln: Untersuchung des Betriebsverhaltens nasslaufender Lamellenkupplungen bei hoeheren Relativdrehzahlen*; Final Report; FVA: Frankfurt am Main, Germany, 1991.
38. Schade, C.W. *Effects of Transmission Fluid on Clutch Performance*; SAE Technical Paper; SAE: Warrendale, PA, USA, 1971; No. 710734. [[CrossRef](#)]
39. Lloyd, F.A. *Parameters Contributing to Power Loss in Disengaged Wet Clutches*; SAE Technical Paper; SAE: Warrendale, PA, USA, 1974; No. 740676. [[CrossRef](#)]
40. Beisel, W.; Federn, K. *FVA No. 53/I—Reibflächenausführung: Untersuchung des Einflusses von Reibflächen-Profil und Oberflächenqualität der Sinterbelag-Lamellen im Hinblick auf den Drehmomentverlauf und die Belastbarkeit, sowie auf das Leerlaufmoment nasslaufender Reibungskupplungen*; Final Report; FVA: Frankfurt am Main, Germany, 1981.
41. Beisel, W.; Federn, K. *FVA No. 53/II—Lamellenwellung: Untersuchung des Einflusses einer Sinuswellung der Stahllamellen auf das Leerlaufverhalten von Lamellenkupplungen mit der Reibpaarung Stahl/Sinterbronze bei unterschiedlicher Reibflächengestaltung*; Final Report; FVA: Frankfurt am Main, Germany, 1982.
42. Fish, R.L. *Using the SAE #2 Machine to Evaluate Wet Clutch Drag Losses*; SAE Technical Paper; SAE: Warrendale, PA, USA, 1991; No. 910803. [[CrossRef](#)]
43. Friedrich, O.; Funk, W. *FVA No. 117/III—Lamellen mit schraeggestellter Achse: Verhalten von Lamellenpaketen groesserer Reibflaechenanzahl bei nichthorizontalem Einbau waehrend des Leerlaufs*; Final Report; FVA: Frankfurt am Main, Germany, 1991.
44. Razzaque, M.M.; Kato, T. Effects of Groove Orientation on Hydrodynamic Behavior of Wet Clutch Coolant Films. *J. Tribol.* **1999**, *121*, 56–61. [[CrossRef](#)]
45. Kitabayashi, H.; Li, C.Y.; Hiraki, H. *Analysis of the Various Factors Affecting Drag Torque in Multiple-Plate Wet Clutches*; SAE Technical Paper; SAE: Warrendale, PA, USA, 2003; No. 2003-01-1973. [[CrossRef](#)]
46. Aphale, C.R.; Cho, J.; Schultz, W.W.; Ceccio, S.L.; Yoshioka, T.; Hiraki, H. Modeling and Parametric Study of Torque in Open Clutch Plates. *J. Tribol.* **2006**, *128*, 422–430. [[CrossRef](#)]
47. Hu, J.; Peng, Z.; Yuan, S. Drag Torque Prediction Model for the Wet Clutches. *Chin. J. Mech. Eng.* **2009**, *22*, 238–243. [[CrossRef](#)]
48. Yuan, S.; Guo, K.; Hu, J.; Peng, Z. Study on Aeration for Disengaged Wet Clutches Using a Two-Phase Flow Model. *J. Fluids Eng.* **2010**, *132*, 111304. [[CrossRef](#)]
49. Aphale, C.R.; Schultz, W.W.; Ceccio, S.L. Aeration in Lubrication With Application to Drag Torque Reduction. *J. Tribol.* **2011**, *133*, 031701. [[CrossRef](#)]
50. Jammulamadaka, A.K.; Gaokar, P. Spin Loss Computation for Open Clutch Using CFD. *SAE Int. J. Engines* **2011**, *4*, 1536–1544. [[CrossRef](#)]
51. Rudloff, M.; Bartel, D.; Deters, L. Simulation der Strömung in nasslaufenden Lamellenkupplungen. In *Kupplungen und Kupplungssysteme 2011*; VDI, Ed.; VDI Verlag: Düsseldorf, Germany, 2011; pp. 177–186.
52. Takagi, Y.; Okano, Y.; Miyagawa, M.; Katayama, N. Combined Numerical and Experimental Study on Drag Torque in a Wet Clutch. In *Proceedings of the ASME-JSME-KSME 2011 Joint Fluids Engineering Conference, Hamamatsu, Japan, 24–29 July 2011*; pp. 2425–2430, ISBN 978-0-7918-4440-3.
53. Madhavan, J.; Pandit, G.; Barnholt, M.; Suppiger, R. *Application of Simulation Based Methods in Development of Wet Clutch System*; SAE Technical Paper; SAE: Warrendale, PA, USA, 2012; No. 2012-28-0022. [[CrossRef](#)]
54. Li, H.; Jing, Q.; Ma, B. Modeling and Parametric Study on Drag Torque of Wet Clutch. In *Proceedings of the FISITA 2012 World Automotive Congress*; Springer: Berlin/Heidelberg, Germany, 2013; pp. 21–30, ISBN 978-3-642-33743-7.
55. Iqbal, S.; Al-Bender, F.; Pluymers, B.; Desmet, W. Model for Predicting Drag Torque in Open Multi-Disks Wet Clutches. *J. Fluids Eng.* **2014**, *136*, 021103. [[CrossRef](#)]

56. Pahlovy, S.A.; Mahmud, S.F.; Kubota, M.; Ogawa, M.; Takakura, N. Multiphase Drag Modeling for Prediction of the Drag Torque Characteristics in Disengaged Wet Clutches. *SAE Int. J. Commer. Veh.* **2014**, *7*, 441–447. [[CrossRef](#)]
57. Sung, I.-H.; Seok, R.J. Computational Simulation Study on the Viscous Drag of the Automotive Wet Clutch for Prediction and Control. In *Advances in Multidisciplinary Engineering*; Jahanmir, S., Saka, N., Tucker, C., Kim, S.-G., Eds.; ASME Press: New York, NY, USA, 2016; pp. 43–48, ISBN 9780791861080.
58. Wu, W.; Xiong, Z.; Hu, J.; Yuan, S. Application of CFD to model oil–air flow in a grooved two-disc system. *Int. J. Heat Mass. Transf.* **2015**, *91*, 293–301. [[CrossRef](#)]
59. Draexl, T.; Pflaum, H.; Stahl, K. FVA No. 671/I—Schleppverluste Lamellenkupplungen II: Wirkungsgradverbesserung durch Reduzierung der Schleppverluste an Lamellenkupplungen; Final Report; FVA: Frankfurt am Main, Germany, 2016.
60. Pahlovy, S.A.; Mahmud, S.F.; Kubota, M.; Ogawa, M.; Takakura, N. *Development of an Analytical Model for Prediction of Drag Torque Characteristics of Disengaged Wet Clutches in High Speed Region*; SAE Technical Paper; SAE: Warrendale, PA, USA, 2017; No. 2017-01-1132. [[CrossRef](#)]
61. Wang, P.; Katopodes, N.; Fujii, Y. Two-Phase MRF Model for Wet Clutch Drag Simulation. *SAE Int. J. Engines* **2017**, *10*, 1327–1337. [[CrossRef](#)]
62. Asai, K.; Ito, T. *Effect of Facing Groove Design on Drag Torque of Automatic Transmission Wet Clutches*; SAE Technical Paper; SAE: Warrendale, PA, USA, 2018; No. 2018-01-0400. [[CrossRef](#)]
63. Hu, J.; Hou, S.; Wei, C. Drag torque modeling at high circumferential speed in open wet clutches considering plate wobble and mechanical contact. *Tribol. Int.* **2018**, *124*, 102–116. [[CrossRef](#)]
64. Pahlovy, S.A.; Mahmud, S.; Ogawa, M. *Development of New Groove Design for Reduction of Drag Torque or Spin Loss of Disengaged Wet Clutches in the High Speed Region*; SAE Technical Paper; SAE: Warrendale, PA, USA, 2018; No. 2018-01-1300. [[CrossRef](#)]
65. Wu, P.; Zhou, X.; Yang, C.; Lv, H.; Lin, T.; Wu, X. Parametric analysis of the drag torque model of wet multi-plate friction clutch with groove consideration. *Ind. Lubr. Tribol.* **2018**, *70*, 1268–1281. [[CrossRef](#)]
66. Bin, W.; Yongyong, H.; Wei, W.; Jianbin, L. Simulation and experiment of viscous torque for disengaged wet clutches of tracked vehicle. *Proc. Inst. Mech. Eng. Part J J. Eng. Tribol.* **2019**, *233*, 593–604. [[CrossRef](#)]
67. Groetsch, D.; Niedenthal, R.; Voelkel, K.; Pflaum, H.; Stahl, K. Effiziente CFD-Simulationen zur Berechnung des Schleppmoments nasslaufender Lamellenkupplungen im Abgleich mit Prüfstandmessungen. *Forsch Ingenieurwes* **2019**, *83*, 227–237. [[CrossRef](#)]
68. Leighton, M.; Morris, N.; Trimmer, G.; King, P.D.; Rahnejat, H. Efficiency of disengaged wet brake packs. *Proc. Inst. Mech. Eng. Part D J. Automob. Eng.* **2019**, *233*, 1562–1569. [[CrossRef](#)]
69. Li, C.; Wu, W.; Liu, Y.; Hu, C.; Zhou, J. Analysis of Air-Oil Flow and Heat Transfer inside a Grooved Rotating-Disk System. *Processes* **2019**, *7*, 632. [[CrossRef](#)]
70. Luo, T.; Li, Z.; Li, F. Drag Characteristics Prediction for Wet Multi-Disk Brakes. *J. Beijing Inst. Technol.* **2019**, *28*, 549–560. [[CrossRef](#)]
71. Morris, N.; Davies, J.; Leighton, M.; King, P.D.; Rahnejat, H. Oil film separation and drag torque in disengaged wet brakes. *Proc. Inst. Mech. Eng. Part D J. Automob. Eng.* **2019**, *233*, 095440701984435. [[CrossRef](#)]
72. Pan, H.; Zhou, X. Experimental and Theoretical Analysis of the Drag Torque in Wet Clutches. *Fluid Dyn. Mater. Process.* **2019**, *15*, 403–417. [[CrossRef](#)]
73. Peng, Z.; Yuan, S. Mathematical Model of Drag Torque with Surface Tension in Single-Plate Wet Clutch. *Chin. J. Mech. Eng.* **2019**, *32*, 25. [[CrossRef](#)]
74. Wang, Y.; Ren, S.; Li, Y. Modeling of the drag torque of the disengaged grooved wet clutches with waviness. *Proc. Inst. Mech. Eng. Part J J. Eng. Tribol.* **2019**, *233*, 1059–1067. [[CrossRef](#)]
75. Zhang, L.; Wei, C.; Hu, J.B. Model for the prediction of drag torque characteristics in wet clutch with radial grooves. *Proc. Inst. Mech. Eng. Part D J. Automob. Eng.* **2018**, *49*, 095440701881495. [[CrossRef](#)]
76. Zhang, L.; Wei, C.; Hu, J.; Hu, Q. Influences of lubrication flow rates on critical speed of rub-impact at high circumferential velocities in No-Load multi-plate wet clutch. *Tribol. Int.* **2019**, *140*, 105847. [[CrossRef](#)]
77. Groetsch, D.; Niedenthal, R.; Voelkel, K.; Pflaum, H.; Stahl, K. *Volume of Fluid vs. Cavitation CFD-Models to Calculate Drag Torque in Multi-Plate Clutches*; SAE Technical Paper; SAE: Warrendale, PA, USA, 2020; No. 2020-01-0495. [[CrossRef](#)]
78. Morris, N.J.; Patel, R.; Rahnejat, H. Hydrodynamic Lubricant Film Separation During Codirectional and Counter-Directional Rotations of Disengaged Wet Clutch Packs. *J. Fluids Eng.* **2020**, *142*, 011104. [[CrossRef](#)]
79. Rogkas, N.; Spitas, V. Investigation of the effect of non-uniform discs clearance on the drag torque of a DCT wet friction clutch. In Proceedings of the ISMA 2020, International Conference on Noise and Vibration Engineering/USD 2020, International Conference on Uncertainty in Structural Dynamics, Leuven, Belgium, 7–9 September 2020; KU Leuven Department of Mechanical Engineering: Heverlee, Belgium, 2020; pp. 3799–3810, ISBN 978-90-828931-1-3.
80. Neupert, T.; Bartel, D. Measurement of pressure distribution and hydrodynamic axial forces of wet clutch discs. *Tribol. Int.* **2021**, *163*, 107172. [[CrossRef](#)]
81. Goszczak, J.; Leyko, J.; Mitukiewicz, G.; Batory, D. Experimental Study of Drag Torque between Wet Clutch Discs. *Appl. Sci.* **2022**, *12*, 3900. [[CrossRef](#)]

82. Nasiri, H.; Delprete, C.; Brusa, E.; Razavykia, A.; Esmaeilzadeh, A. Analytical simulation of influential parameters affecting grooved wet clutches performance under disengagement condition. *Proc. Inst. Mech. Eng. Part J J. Eng. Tribol.* **2022**, *236*, 1113–1122. [[CrossRef](#)]
83. Pointner-Gabriel, L.; Pflaum, H.; Voelkel, K.; Stahl, K. *FVA No. 671/II—Schleppmomentberechnung: Berechnung der Schleppmomente nasslaufender Lamellenkupplungen*; Final Report; FVA: Frankfurt am Main, Germany, 2022.
84. Xu, C.; Xie, F.; Guo, X.; Agarwal, R.K.; Liu, X.; He, K.; Li, Z. Theoretical and experimental study on drag torque of wet clutch considering surface tension and shrinkage of oil film. *Proc. Inst. Mech. Eng. Part D J. Automob. Eng.* **2022**. [[CrossRef](#)]
85. Guerbuez, H.; Bischofberger, A.; Ott, S. Getriebefedern für einen effizienten und regelbaren Betrieb von Kupplungs- und Bremssystemen in E-Fahrzeugen. *Forsch Ingenieurwes* **2023**, *87*, 529–540. [[CrossRef](#)]
86. Qu, D.; Yun, Y.; Zhao, D. Analysis of Wet Clutch Drag Torque and Optimization of Drag Torque Reduction Measures. In *2023 International Conference on Marine Equipment & Technology and Sustainable Development*; Yang, D., Ed.; Springer Nature: Singapore, 2023; pp. 541–554, ISBN 978-981-99-4290-9.
87. Tan, W.; Chen, Z.; Li, Z.; Yan, H. Thermal-Fluid-Solid Coupling Simulation and Oil Groove Structure Optimization of Wet Friction Clutch for High-Speed Helicopter. *Machines* **2023**, *11*, 296. [[CrossRef](#)]
88. Pointner-Gabriel, L.; Voelkel, K.; Schneider, T.; Stahl, K. *FVA No. 671/III—Schleppmomentberechnung II: Berechnung und Untersuchung der Schleppmomente nasslaufender Lamellenkupplungen*; Final Report; FVA: Frankfurt am Main, Germany, 2024.
89. Pointner-Gabriel, L.; Steiner, M.; Voelkel, K.; Stahl, K. Using Gaussian process regression for building a data-driven drag loss model of wet clutches. *Tribol. Int.* **2024**, *198*, 109825. [[CrossRef](#)]
90. Zhang, L.; Zhang, Y.; Wei, C.; Yan, Y. Optimization Design of Oil Groove Shape on the Surface of Friction Plate in High-Speed Wet Clutch Aimed at Minimizing Drag Torque. *J. Tribol.* **2024**, *146*, 034601. [[CrossRef](#)]
91. Schneider, T.; Bedrikow, A.B.; Voelkel, K.; Pflaum, H.; Stahl, K. Load Capacity Comparison of Different Wet Multi-Plate Clutches with Sinter Friction Lining with Regard to Spontaneous Damage Behavior. *Tribol. Ind.* **2022**, *44*, 394–406. [[CrossRef](#)]
92. Yuan, S.; Peng, Z.; Jing, C. Experimental Research and Mathematical Model of Drag Torque in Single-plate Wet Clutch. *Chin. J. Mech. Eng.* **2011**, *24*, 91–97. [[CrossRef](#)]
93. Leister, R.; Fuchs, T.; Kriegseis, J. Defocusing PTV applied to an open wet clutch: From macro to micro. *Exp. Fluids* **2023**, *64*, 94. [[CrossRef](#)]
94. Albers, A.; Ott, S.; Basiewicz, M.; Denda, C.; Kriegseis, J. Variation von Nutbildern mittels generativer Verfahren zur Untersuchung von Schleppverlusten in Lamellenkupplungen. In *Kupplungen und Kupplungssysteme in Antrieben 2017*; VDI, Ed.; VDI Verlag: Düsseldorf, Germany, 2017; pp. 293–300, ISBN 978-3-18-102309-9.
95. Markowsky, F. Echtzeit-Analyse des Trennverhaltens von Lamellenkupplungen: Einfluss auf die Systemfunktion und dessen Reproduzierbarkeit. In *Kupplungen und Kupplungssysteme in Antrieben 2017*; VDI, Ed.; VDI Verlag: Düsseldorf, Germany, 2017; pp. 125–134, ISBN 978-3-18-102309-9.
96. Pointner-Gabriel, L.; Flamm, S.; Schneider, T.; Stahl, K. A methodology for image-based measurement of plate movement in disengaged wet clutches. *Sci. Rep.* **2024**, *14*, 7631. [[CrossRef](#)]
97. Wang, P.; Katopodes, N.; Fujii, Y. Statistical Modeling of Plate Clearance Distribution for Wet Clutch Drag Analysis. *SAE Int. J. Passeng. Cars Mech. Syst.* **2018**, *11*, 76–88. [[CrossRef](#)]
98. Pahlovy, S.A.; Mahmud, S.F.; Kubota, M.; Ogawa, M.; Takakura, N. New Development of a Gas Cavitation Model for Evaluation of Drag Torque Characteristics in Disengaged Wet Clutches. *SAE Int. J. Engines* **2016**, *9*, 1910–1915. [[CrossRef](#)]
99. Leister, R.; Pasch, S.; Kriegseis, J. On the applicability of LDV profile-sensors for periodic open wet clutch flow scenarios. *Exp. Fluids* **2022**, *63*, 134. [[CrossRef](#)]
100. Pardeshi, I.; Shih, T.I.-P. Modeling Gas–Liquid Flow Between Rotating and Nonrotating Annular Disks. *J. Fluids Eng.* **2019**, *141*, 121303. [[CrossRef](#)]
101. Pan, H.; Zhou, X. Simulation Research on the Drag Torque of Disengaged Wet Clutches. In *Proceedings of the 2019 IEEE 5th International Conference on Mechatronics System and Robots (ICMSR)*, Singapore, 3–5 May 2019; pp. 44–48. [[CrossRef](#)]
102. Leister, R.; Najafi, A.F.; Gatti, D.; Kriegseis, J.; Frohnäpfel, B. Non-dimensional characteristics of open wet clutches for advanced drag torque and aeration predictions. *Tribol. Int.* **2020**, *152*, 106442. [[CrossRef](#)]
103. Leister, R.; Najafi, A.F.; Kriegseis, J.; Frohnäpfel, B.; Gatti, D. Analytical modeling and dimensionless characteristics of open wet clutches in consideration of gravity. *Forsch Ingenieurwes* **2021**, *85*, 849–857. [[CrossRef](#)]
104. Tarasow, A.; Tilly, J.V.G.; Arndt, T.; Neudecker, B.; Serway, R. Adaptive Ermittlung des viskosen Reibmoments bei hydraulisch betätigten Nasskupplungen. In *AUTOREG 2017*; VDI, Ed.; VDI Verlag: Düsseldorf, Germany, 2017; pp. 273–286, ISBN 9783181022924.
105. Pardeshi, I.; Shih, T.I.-P. A Computational Fluid Dynamics Methodology for Predicting Aeration in Wet Friction Clutches. *J. Fluids Eng.* **2019**, *141*, 121304. [[CrossRef](#)]
106. Zhang, M.; Liu, Y.; Liu, T.; Xu, X.; Xu, J.; Zhang, Y. The drag characteristics prediction of multi-plate frictional wet clutches in vehicle transmissions. *J. Mech. Sci. Technol.* **2023**, *37*, 3249–3259. [[CrossRef](#)]

-
107. Hirt, C.; Nichols, B. Volume of fluid (VOF) method for the dynamics of free boundaries. *J. Comput. Phys.* **1981**, *39*, 201–225. [[CrossRef](#)]
 108. Singhal, A.K.; Athavale, M.M.; Li, H.; Jiang, Y. Mathematical Basis and Validation of the Full Cavitation Model. *J. Fluids Eng.* **2002**, *124*, 617–624. [[CrossRef](#)]

Disclaimer/Publisher’s Note: The statements, opinions and data contained in all publications are solely those of the individual author(s) and contributor(s) and not of MDPI and/or the editor(s). MDPI and/or the editor(s) disclaim responsibility for any injury to people or property resulting from any ideas, methods, instructions or products referred to in the content.